공학박사 학위논문

Polarization control of
surface plasmon polaritons and
its application to polarimeter

표면 플라즈몬 폴라리톤의 편광 제어 방법과

편광측정기에의 응용

2017년 8월

서울대학교 대학원

전기·컴퓨터공학부

이 규 근

Abstract

Polarization control of surface plasmon polaritons and its application to polarimeter

Kyookeun Lee

Department of Electrical Engineering and Computer Science

College of Engineering

Seoul National University

Surface plasmon polaritons (SPPs) are electromagnetic waves propagating along the metal-dielectric interface. Plasmonics has been rigorously studied over the last decade, since SPPs are considered as one of the most promising candidates to accomplish highly integrated photonic circuits with their unique ability to squeeze light under the diffraction limit. Among various efforts to develop plasmonic elements in both passive and active ways, it is still a crucial issue how to generate SPPs with high coupling efficiency. Recently, nano-antennas with asymmetric structures have been showing that they could give directivity to generation of SPPs, so that the coupling efficiency could be more enhanced. In addition to directional excitation of SPPs, control of the direction attracts research interests in terms of plasmonic routers and multiplexed plasmonic elements. The polarization states of incident light is an adequate component to be a control signal, making use of polarization-selective nature of both SPPs and anisotropic scatterers. However, controllability of previous studies is bounded by binary operation in general with respect to the helicity or the orientation angle of the incident light.

This dissertation investigates polarization control of SPPs and their application to a compact polarimeter. The controllability of SPPs is extended based on periodic nano-aperture arrays and polarized light, and their

applications are suggested.

First, the issue of interferometric-controlled optical devices is discussed. Interaction between light and optical devices can be tuned in all-optical manner with high modulation depth by controlling interference of coherent light. When two parallel arrays of aperture pairs are illuminated by linearly polarized light, interference of counter-propagating SPPs excited by the arrays can be controlled by the orientation angle of the incident light. Translation of optical path length can be replaced by the orientation angle rotation of the incident field. This makes experimental setup of the interferometry be significantly simplified.

The second application deals with a compact polarimeter, an optical analyzer that detects the state of polarization (SOP). In order to measure the full-Stokes parameters, polarizers with different measuring SOPs are required. Polarization-selective excitation of SPPs can play a role of a polarizer since the selective excitation implies that SPPs are extinguished at a certain polarization. Hybrid aperture pair array and X-shaped aperture array are proposed to launch SPPs to a single direction when illuminated by the target elliptical SOP. Then, the aperture arrays are applied to the polarimeter, which are equivalent to four different elliptical polarizers. Polarization states can be measured at a single shot detection within a tiny system.

I expect that this dissertation can help to develop more compact optical systems based on polarization-sensitive optical elements. Furthermore, I hope that this work inspires research on optical angular momentum interaction mediated by nano-structures surface waves.

Contents

iv

List of Tables

List of Figures

Chapter 1 Introduction

1.1 Overview of plasmonics

Surface plasmon polaritons (SPPs) are electromagnetic waves propagating along the metal-dielectric interface. Plasmonics has been rigorously studied over the last decade since SPPs are nominated as one of the most promising candidates to accomplish highly integrated photonic circuits with their unique ability to squeeze light under the diffraction limit [1, 2]. Plasmonic waveguides, for example, can deliver guided modes with volume of smaller than a few tens of nanometers, while photonic modes are cut off [3, 4]. As well as various types of waveguides [5–7], other plasmonic elements including resonators [8–11] and interconnectors [12–14] have been successfully demonstrated, thanks to the rapid development of nanofabrication techniques. Active plasmonic devices, which modulate SPPs using external control signals such as sources [15–20], amplifiers [21, 22], modulators [23–27], switches [28–31], and logic gates [32, 33], have also been proposed based on electro-optical, thermo-optical, mechanical, and all-optical mechanisms.

Among various efforts to develop plasmonic elements in both passive and active ways, it is still a crucial issue how to generate SPPs with high efficiency. Because of higher momentum of SPPs than free space photons,

additional apparatus is required to couple incident light into SPPs. Prisms and gratings are typical examples. At the early stage of research, optical nano-antennas were proposed, adopted from advanced radiofrequency antenna theories [34–36]. Especially, nano-antennas with asymmetric structure give directivity to generation of SPPs, so that the coupling efficiency can be more enhanced [37–41].

More recent studies on SPP couplers suggest control of directivity, as well as directional coupling of SPPs with high extinction ratio. Polarization states of incident light is widely utilized as a control signal, making use of polarization-selective nature of both SPPs and anisotropic scatterers. Fully perforated slits and apertures [42–47], asymmetric nano-antennas [48, 49], and waveguides [50] are applied to directional launching and switching of SPPs with the control of the linear and circular polarization states of the incident light. In terms of integrated plasmonic circuits, directional control of SPPs can also be utilized as plasmonic routers and multiplexed elements.

Furthermore, interaction between circularly polarized light and anisotropic scattering of SPPs can help to explore spin-orbit interaction of light based on subwavelength nano-structures. Since the circularly polarized light carries an intrinsic spin angular momentum, spatially inhomogeneous media can cause spin-dependent phenomena [51]. Generation and control of plasmonic vortex fields using the spin or geometry of the plasmonic structure are a proper instance that shows the spin-orbit interaction of light. Observation of the spin-orbit interaction is experimentally presented by plasmonic vortex lenses with geometry of the Archimedean spiral [52] and chains of anisotropic nano-apertures [53, 54].

1.2 Motivation of this dissertation

Excitation of SPPs using periodic array of anisotropic scatterer is a powerful platform that tailors wavefront of SPPs. When light is incident with a certain state of polarization (SOP), amplitude and phase profile of the generated SPPs can be designed by a position and a tilt angle of each scatterers. Recently, polarization-controlled SPP excitation was demonstrated using an array of rectangular nano-aperture pairs [46]. Both pathway and phase of excited SPPs can be tuned independently by changing positions and tilt angles of the apertures. Plasmonic elements of multiplexed-lenses [49, 55–57] and caustic beam generator [58] have been demonstrated, applying the proposed working principle. These applications show possibilities of excitation and control of SPPs based on the aperture pair array. However, controllability of the previous studies are bounded by binary operation with respect to the helicity of the incident light. In this dissertation, the controllability of SPPs based on the aperture arrays is extended and its applications are presented.

The first application focuses on the issue of interferometric-controlled optical devices. All-optic control utilizing interference between independent coherent light sources provides controllability of nanostructured optical devices. Interaction between light and optical devices can be tuned in all-optical manner with high modulation depth by controlling interference of coherent sources. For example, resonators with lossy media illuminated by coherent light sources can absorb light perfectly, which corresponds to time-reversal process of lasing [59, 60]. In addition to absorption, reflection and

transmission are actively tuned by controlling the phase difference of incoming coherent light [61–63]. However, an experimental apparatus to realize optical coherent control systems requires delicate alignment of optical elements and fine control of optical path length. In the visible and the near-infrared regime in particular, change of optical path length by a few tens of nanometers influences the result considerably. Interferometric control of SPPs using the aperture arrays can manage this issue. When two parallel arrays of the aperture pairs are illuminated by linearly polarized light, interference between counter-propagating SPPs excited by the arrays can be controlled by the orientation angle of the incident light. Translation of optical path length is then replaced by the orientation angle rotation of the incident field. Hence, experimental setup of the interferometry can be significantly simplified.

The second application deals with a compact polarimeter based on polarization-sensitive generation of SPPs. Polarimeter is an optical analyzer that detects the SOP. Typically, SOPs are obtained after several times of measurements by branching the input beam either spatially [64] or temporally [65]. This measurement scheme makes the polarimeter be bulky and sluggish. With help of recent advances in nanophotonics, several efforts have been made that introduce compact polarimeters. Various types of circular polarization analyzers that measure the helicity of light have been proposed based on spin-dependent scattering of light [66–70]. Full-Stokes polarimeters based on plasmonic elements [69, 70], metasurfaces [71, 72], and asymmetric silicon waveguides [73] have been demonstrated. States of polarizations are fully specified by a single measurement without any

4
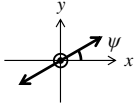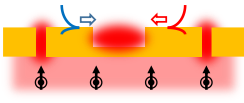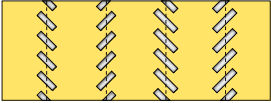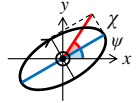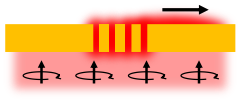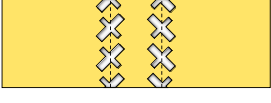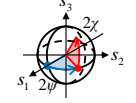
splitting of optical paths using proposed polarimeters. However, in these studies, polarimeters are designed at certain target wavelengths, so that operation bandwidths are limited. Recently, spectropolarimeters, which measure both the wavelength and the SOP simultaneously with broad operation bandwidths, were presented using chromatic aberrations of metasurfaces [74, 75]. Measurement accuracy of these metasurface-based polarimeters, however, is dependent on propagation length of probing signals, since the working principle relies on polarization-dependent deflection.

A polarimeter composed of polarization-sensitive excitation of SPPs can help to improve the aforementioned issues. In order to measure the full-Stokes parameters, polarizers with different measuring SOPs are required. Polarization-selective excitation of SPPs can play a role of a polarizer since the selective excitation implies that SPPs are extinguished at a certain polarization. In order to reduce the number of measuring polarizers and use the optimized measurement scheme, four different elliptical polarizers are needed. Directional launching of SPPs using elliptical polarized light has been reported based on asymmetric nano-spheres [76]. However, the proposed device is hard to implement because the nano-sphere should be floated from the surface with the exact geometry. This problem is handled by introducing novel aperture pair array. Proposed aperture array launches SPPs to a single direction with high extinction ratio when illuminated by the target elliptical SOP. Then, the aperture pair arrays are applied to polarimeter, which are equivalent to four different elliptical polarizers. Polarization states can be measured at a single shot detection within a tiny system.

1.3 Scope and organization

This dissertation describes methods for polarization control of SPPs and its application to a compact polarimeter. Structure of aperture pair array perforated on a metal film and its interaction with polarized light is one of the main subject in this dissertation. At the beginning, basic physics of SPPs and excitation mechanism of SPPs at a periodic aperture array will be explained briefly. Then detailed descriptions of each chapter will be presented in following order: introduction, working principles, design and simulation results, experimental results, and summary with discussions.

Table 1.1 Main subjects of each chapter in terms of aperture geometries, incident polarization states, and functions of the devices.

Chapter	Aperture array geometry (xy-plane)	Incident polarization states	Function of the device
3	■ Facing aperture pairs	■ Linear	■ Interferometric control
4	■ Hybrid aperture pair	■ Elliptical	■ Directional control
5	■ X-shaped aperture pair	■ Arbitrary	■ Measurement of SOPs

In Chapter 3, polarization control of an SPP interference will be described. An orientation angle of an incident field is used as a control signal

here. Working principle based on rectangular aperture pair arrays in face-to-face arrangement will be explained in Section 3.2. Optimization results of a rectangular plasmonic resonator, which is controlled by interference of SPPs, will be presented in Section 3.3. After that, experimental results based on near-field scanning optical microscopy (NSOM) will be shown in Section 3.4.

In Chapter 4, directional launching and switching of SPPs will be explained. Excitation of SPPs at a hybrid aperture pair array illuminated by elliptically polarized light will be discussed in Section 4.2. Conditions for directional generation of SPPs and its switching are yielded from a simple analytic model based on superposition of complex fields. In Section 4.3, extinction ratio of fabricated hybrid aperture pair array is measured.

In Chapter 5, a compact plasmonic polarimeter will be proposed. At first, an X-shaped aperture array will be introduced in Section 5.2 as a building block of the polarimeter. It will be shown that the X-shaped aperture array is an elliptical polarizer with broad operation wavelength range. In Section 5.3, configuration of the polarimeter will be presented using the X-shaped aperture arrays. It will be explained that an arbitrary SOP can be specified by detecting four SPP intensities with calibration factors. In Section 5.4, Experimental results will verify operation of the proposed polarimeter at wavelengths of 800 nm, 840 nm, 920 nm, and 980 nm.

Chapter 6 will give summary of this dissertation and concluding remarks with perspectives.

Chapter 2 Interaction between polarized light and plasmonic nano-structures

2.1 Propagation of SPPs at a metal-dielectric single interface

Throughout this dissertation, SPPs propagating along the metal-air interface is mainly discussed. Therefore, it will be helpful to start with brief introduction to SPPs at the single interface geometry.

Consider a geometry that homogeneous metal (ε_m) and air make a contact locating the interface at $z = 0$. Source-free Maxwell's equation and boundary conditions at the interface yield non-zero solution of a transverse-magnetic mode when sign of permittivity of the given geometry changes at $z = 0$. Field profiles of achieved electromagnetic waves in the area of $z > 0$ are written as [77]:

$$\mathbf{H} = \left(0, H_0, 0\right) e^{j k_{\mathrm{SPP}} x} e^{-\kappa_d z} , \tag{2.1}$$

$$\mathbf{E} = \frac{H_0}{\omega \varepsilon_0} \left(j\kappa_d, 0, -k_{\mathrm{SPP}} \right) e^{jk_{\mathrm{SPP}}x} e^{-\kappa_d z}, \qquad (2.2)$$

where ω is angular frequency, ε_0 vacuum permittivity. κ_d and k_{SPP} are wave vector component to the x-axis and z-axis, respectively. In the area of $z < 0$, similarly,

$$\mathbf{H} = \left(0, H_0, 0 \right) e^{jk_{\mathrm{SPP}}x} e^{\kappa_m z}, \qquad (2.3)$$

$$\mathbf{E} = \frac{H_0}{\omega \varepsilon_0 \varepsilon_m} \left(-j\kappa_m, 0, -k_{\mathrm{SPP}} \right) e^{jk_{\mathrm{SPP}}x} e^{\kappa_m z}. \qquad (2.4)$$
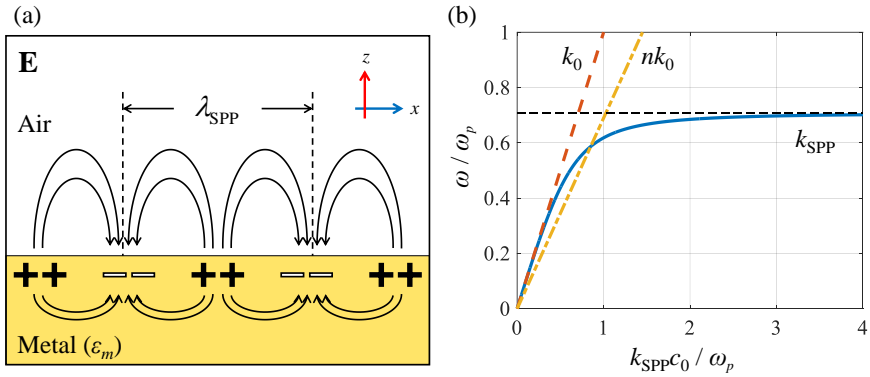
Figure 2.1 (a) Schematic illustration of electric fields of SPPs at a metal-air interface. (b) Dispersion relation of SPPs.

Continuity relation at the boundary and wave vector relation yields k_{SPP}, which is a dispersion relation of SPPs:

$$k_{\mathrm{SPP}} = k_0 \sqrt{\frac{\varepsilon_m}{\varepsilon_m + 1}} \ . \tag{2.5}$$

Figure 2.1(b) shows the dispersion relation of SPPs at the interface between a Drude metal with negligible collision frequency and air. A dashed line is that of air and a dash-dotted line is of dielectric medium with refractive index of 1.45. It is shown that SPPs have larger momentum than photons in free space by comparing the dashed line and a solid curve. This implies that SPPs cannot be directly excited by free space photons. Prisms and gratings are typical examples of additional geometry that makes SPPs excited by compensating the phase mismatch.
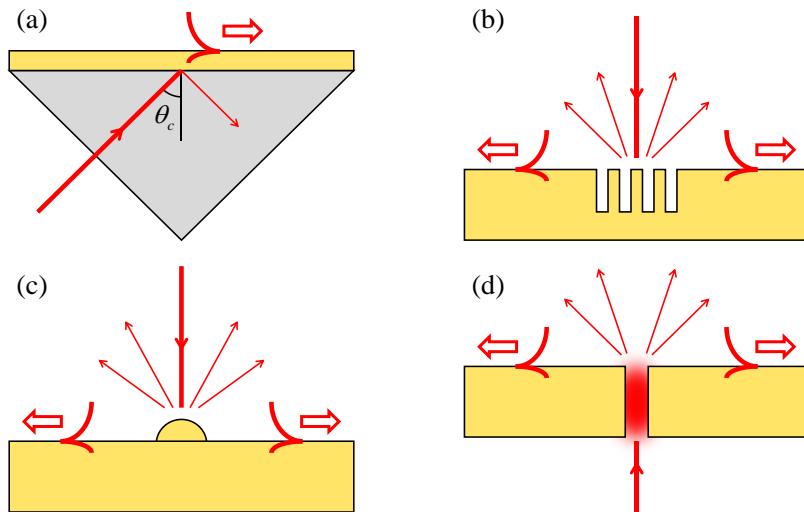
Figure 2.2 Examples of geometries that excite SPPs: (a) a prism (Kretschmann configuration), (b) gratings, (c) a bump/rod, and (d) an aperture.

2.2 Interaction between polarized light and periodic array of plasmonic nano-structures

2.2.1 Tailoring of transmitted/reflected light using plasmonic nano-structure arrays

After the first observation of the extraordinary optical transmission through metallic films perforated by subwavelength hole arrays in 1998 [78], periodic array of subwavelength structures has been one of the most actively studied subjects in photonics. Nanophotonics is coined, meaning a study of photonics utilizing nano-scale functional elements to manipulate light. Transmission, reflection and absorption spectra are engineered using various types of subwavelength periodic arrays with different unit cell geometries, holes, rectangular apertures, c-shaped apertures, dolmen-shaped rods, and asymmetric rings for examples [79–81]. Theoretical approach showed that optical phenomena of periodic array of subwavelength holes can be characterized by scattering of SPP modes [82].

Recently, periodic arrays of plasmonic nano-structures have been applied to spatial modulation of light, attracting much of research interests. Phase and amplitude of an incident wavefront can be fully modulated without any diffraction when the period of scatterers is shorter than wavelength of the given light. Plasmonic nano-structure is widely used as a scatterer due to its large scattering cross section near the resonance. Spatial phase modulation of light is demonstrated firstly using V-shape metallic nano-rods [83]. Phase of scattered fields by the V-shaped nano-rod array can

be modulated from 0 to 2π by engineering arm lengths and angles between the arms. Similarly, T-shaped nano-rod arrays are proposed achieving ultra-thin wave plates [84]. Geometric parameters of widths and lengths of each arm are adjusted. Anomalous reflection is experimentally demonstrated based on a gap-plasmon antenna array with different aspect ratios of the antennas [85]. In these cases, phase of incoming light is manipulated by changing geometric parameters or dispersions of scatterers.
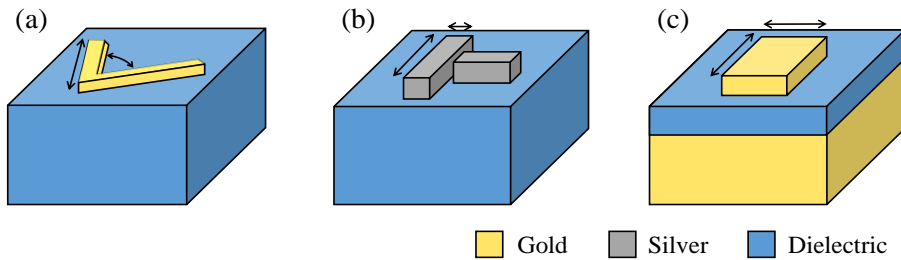
Figure 2.3 Unit cell geometries of plasmonic nano-structure arrays utilizing scatterer dispersions: (a) a V-shaped nano-rod [83], (b) a T-shaped nano-rod [84], and (c) a gap-plasmon antenna [85].
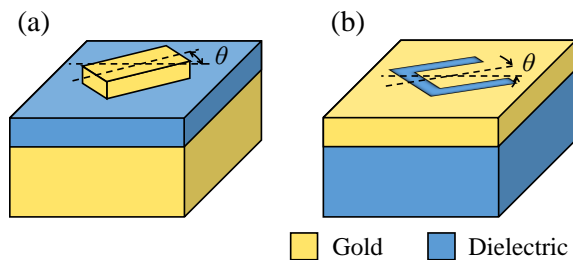
Figure 2.4. Unit cell geometries of plasmonic nano-structure arrays utilizing rotation of anisotropic scatterers: (a) a gap-plasmon antenna [87] and (b) C-shaped aperture with rotation angle of θ [88].

Using circularly polarized light and array of anisotropic scatterers, it is possible to modulate light with the fixed geometry of the scatterer. When circularly polarized light illuminates the anisotropic scatterer array, phase of the cross-polarization component is proportional to $-2\sigma_{in}\theta$, where θ is rotation angle of the scatterer [86]. Helicity of the incident light, σ_{in}, is 1 for the right-hand circular polarization (RCP) and -1 for left-hand circular polarization (LCP). Holograms are demonstrated by modulation phase of reflected light using the geometric phase of rectangular gap-plasmon antenna arrays [87].

In a case of linearly polarized light, amplitude modulation of light can be achieved using two orthogonal polarization states. Amplitude of cross-polarized component changes in a sinusoidal manner according to angle difference between the scatterer and the orientation angle of the incident field, similar to transmission characteristics of a linear polarizer. C-shaped aperture array was introduced that generates Airy beams [88].

2.2.2 Generation and control of SPPs using nano-aperture arrays

In a similar way, optical near-fields delivered by SPPs can be generated and tailored by periodic nano-structures. Rectangular nano-aperture with high aspect ratio is one of the elementary anisotropic antenna of SPPs due to its simple geometry and analytic model. The rectangular aperture radiating SPPs can be modeled as an in-plane dipole source of SPPs [89]. Figure 2.5(b) shows a radiation pattern of SPPs through the rectangular aperture perforated on a gold film. Each level depicts normalized electric field magnitude normal to the surface (E_z-field) with the equal interval at 20 nm above the metal

13

surface. Here, the E_z-field is adopted among field components to represent radiated SPP fields since the E_z-field is only delivered by SPPs while orthogonal to the incident electric field components in this case. Full three-dimensional finite-element method (FEM; COMSOL Multiphysics) is used for the calculation with following parameters: wavelength $\lambda_0 = 980$ nm, dielectric constant of the gold film $\varepsilon_{Au} = -37.81 + j1.13$ [90], refractive index of a substrate $n_{subs} = 1.45$, length and width of the aperture $l = 320$ nm, $w = 80$ nm, and thickness of the film $t_{Au} = 200$ nm.

When periodically arranged rectangular apertures along the y-direction with subwavelength period and the same tilt angle are illuminated by normally incident light, the aperture array generates SPPs with uniform wavefront propagating to the x-direction, as illustrated in Figure 2.5 (a). In this case, Amplitude A and phase profile Φ of the SPP wavefront are determined by the tilt angle of apertures θ. When the input light is circularly polarized, complex field of SPPs $a = A\Phi$ to the $+x$-direction is then approximately written as [58]:

$$a_{x+}\left(\theta\right) = a_0 \sin\theta e^{-j\sigma\theta} , \qquad (2.6)$$

where σ is a helicity of the incident light.
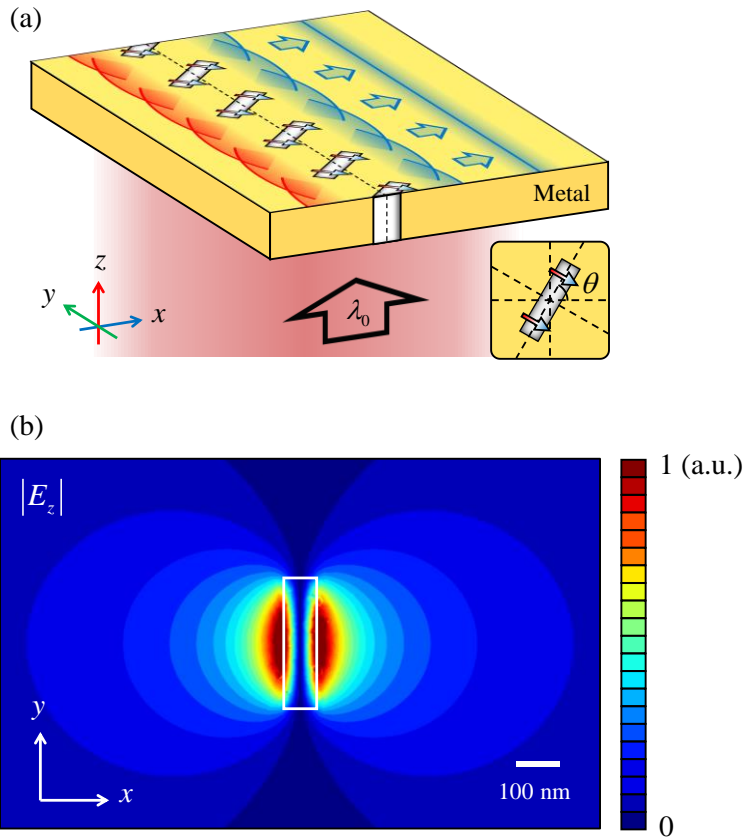
Figure 2.5 (a) Periodically arranged rectangular nano-apertures with tilt angle θ illuminated by normally incident light and (b) scattered field profile of a single rectangular aperture.

Additional column of the aperture array can enlarge the availability of polarization control. When two columns of the aperture array are arranged by face-to-face configuration with a distance of d as seen in Figure 2.6(a), time-averaged SPP intensity to the $+x$-direction is given by:

$$I_{x+}(\theta) = I_0 \sin^2\left(\Delta + \sigma\frac{\pi}{4}\right), \qquad (2.7)$$

where $\Delta = \pi d / \lambda_{SPP}$ is retarded phase due to the distance between the columns.
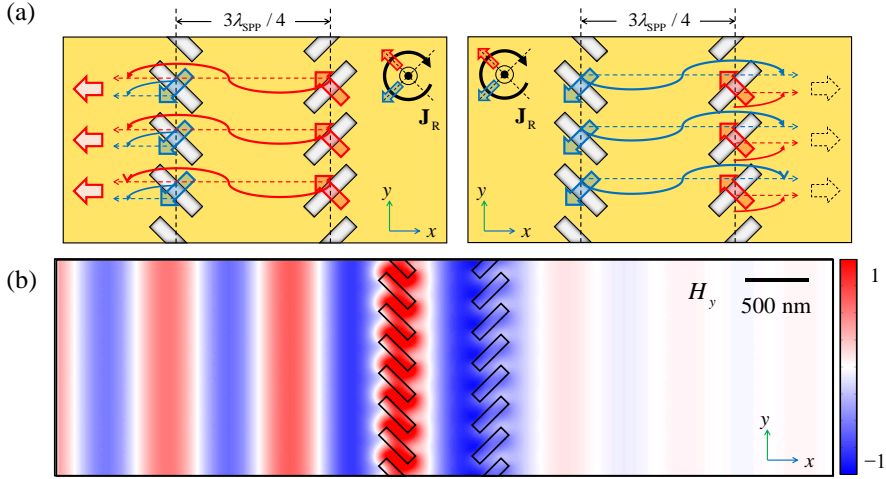
Figure 2.6 (a) Schematic illustration array of rectangular aperture pairs with a distance of $3\lambda_{SPP} / 4$ illuminated by right-hand circularly polarized (RCP) light and (b) its corresponding H_y-field profile.

The intensity becomes zero at a case of $d = 3\lambda_{SPP} / 4$ ($\Delta = 3\pi / 4$) and $\sigma = 1$. That is, SPPs are launched to the single direction of $-x$ when the input beam is the RCP. If the helicity is switched, propagating direction is reversed. Figure 2.6(b) shows simulated SPP field profile of the case. The RCP wave of 980 nm wavelength is normally incident on the aperture array with a period of 240 nm. The distance between the columns is 720 nm, where $\lambda_{SPP} = 976$ nm. Other geometric and physical parameters are the same with the parameters used in Figure 2.5(b). It is clearly seen that SPPs propagate to the

–x-direction.
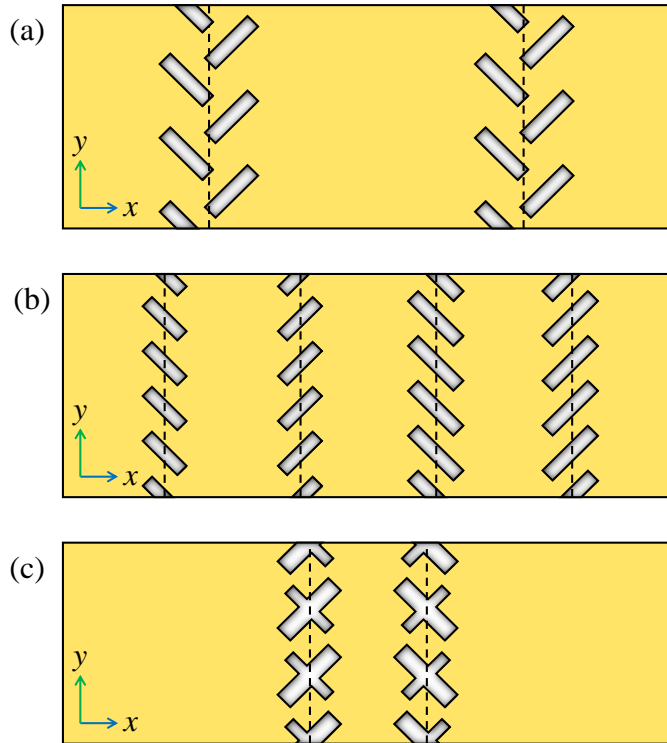
Figure 2.7 Geometries of aperture pair arrays in top-view introduced in this dissertation. (a) Facing aperture pair arrays in Chapter 3, (b) hybrid aperture pair array in Chapter 4, and (c) X-shaped aperture pair array in Chapter 5.

In following chapters, three different types of aperture pair arrays are introduced extending the previously described aperture array: Chapter 3 facing aperture pair arrays, Chapter 4 hybrid aperture pair array, and Chapter 5 X-shaped aperture pair array. Figure 2.7 shows schematic geometries of each array.

The facing aperture pair arrays is composed of two face-to-face-

arranged rectangular aperture pair arrays as shown in Figure 2.7(a). A single line of the array is equivalent to the aperture pair array that is depicted in Figure 2.6. Distance between the adjacent apertures along the x-axis is reduced from $3\lambda_{SPP} / 4$ to $\lambda_{SPP} / 4$. The function of the aperture pair array, polarizing SPP splitting according to the helicity of incoming light, is still valid in this case according to working principle described in Figure 2.6. In order to avoid overlap of apertures, the apertures are arranged like a tire track shape. Two face-to-face-arranged aperture pair arrays can induce interference of SPPs when the arrays are illuminated by normally incident linearly polarized light. More detailed descriptions of its working principle and corresponding function will be presented in Section 3.2.

The hybrid aperture pair array consists of two aperture pair arrays with different openings and rotation angles. Each pair splits SPPs of the RCP and the LCP component of incident light, but with the different direction and coupling coefficient. The hybrid aperture pair array can launch SPPs directionally by elliptically polarized light. Geometric parameters of the aperture pair arrays determine directional launching conditions of SPPs. Effect of widths and lengths of the apertures, and distance between the pair arrays will be discussed in Section 4.2.

The X-shaped aperture pair array can be considered as an overlapped hybrid aperture pair array with zero distance between the pair array. The X-shaped aperture pair reduces the number of geometric parameters, compared to the hybrid aperture pair. Meanwhile, the array gets additional geometric symmetry along the x-axis, which associates with symmetric optical response according to the helicity of an input beam. The X-shaped aperture pair array

18

is equivalent to an elliptical SPP polarizer that extinguishes SPPs when incident light is elliptically polarized. In Chapter 5, a compact polarimeter will be proposed utilizing four different elliptical SPP polarizers composed of the X-shaped aperture pair array.

Chapter 3   Interferometric control of SPPs using linearly polarized light

3.1 Introduction

Surface plasmon polaritons have been successfully applied to building nanoscale optical resonators due to their ability of squeezing light far below the diffraction limit with highly resonant conditions [91]. Subwavelength plasmonic resonators, which are based on single-crystalline silver nanowires [8], few-nanometer-thick metal-insulator-metal waveguides [9], and metallic fins [92], have been demonstrated. Interactions with quantum emitters and lasing action of plasmonic resonators have been also investigated [93–95].

Along with the recent development of active plasmonic elements, tunable plasmonic resonators have been proposed. Thermo-optical and electro-optical control of resonators has been shown using metal strips [96] and graphene nanoribbons [97]. In both cases, material properties of the resonators are tuned by the external control signal. Modulation depth of such active resonators, however, is limited because of small volume of an active layer and short variation range of material properties.

All-optic control utilizing interference between coherent light sources is able to improve the controllability of nanostructured optical devices. Interaction between light and optical devices can be tuned in all-optical

manner with high modulation depth by controlling interference of coherent light [59–63]. However, an experimental apparatus to realize optical coherent control systems requires delicate alignment of optical elements and fine control of optical path length. In the visible and the near-infrared regime in particular, change of the optical path length with a few tens of nanometer influences the result considerably.

Here, a tunable plasmonic resonator is proposed whose property is controlled by linearly polarzed light. The proposed device consists of aperture pair arrays, gratings, and a cavity. The aperture arrays generate and split SPPs into two components when illuminated by linearly polarized light. Phase difference between counter-propagating SPPs is then proportional to the orientation angle of the incident field. This polarization-dependency grants the device tunability. The periodic gratings and the rectangular cavity make a resonator. When the SPPs encounter each other at the resonator with in-phase, electromagnetic energy density in the resonator is maximized. On the other hand, for the out-of-phase case, the energy density is minimized. Utilizing the tunability, absorption and emission can be controlled when the cavity is coupled with lossy media and emitters. After introducing basic principles of interferometric control of SPPs, optimization of the resonator and simulation results will be presented. Experimental results will be shown using the NSOM.

3.2 Face-to-face arrangement of the aperture pair arrays and linearly polarized light incidence
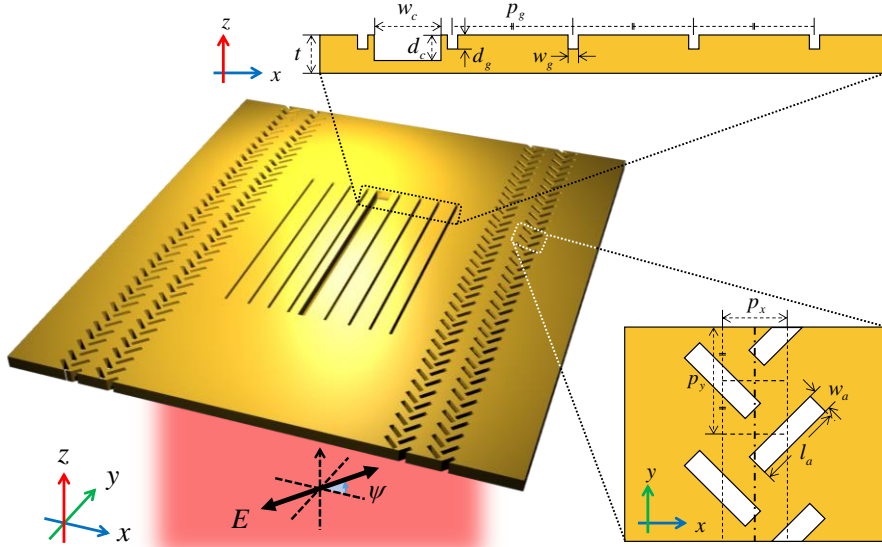
Figure 3.1 Schematic illustration of the overall device. The resonator and the aperture pair arrays are illuminated by the polarized electric field with an orientation angle of ψ. Insets show detailed configuration of the resonator and the aperture pair array.

Figure 3.1 shows a schematic illustration of the proposed device. Configuration of the aperture pair array is shown with details in the inset at the bottom of Figure 3.1. Each geometric parameter indicates: t: metal thickness, w_c: cavity width, d_c: cavity depth, w_g: grating width, d_g: grating depth, p_g: grating period, p_x: x-direction aperture distance, p_y: y-direction aperture period, w_a: aperture width, and l_a: aperture length. A pair of

rectangular apertures, which are tilted with angles of 45 ° at the right side and 135 ° at the left side, are spaced with distance of a quarter wavelength of the SPP. This is the equivalent case explained in the previous section, because translation of sources with a distance of a wavelength will give the same synthesized fields, ignoring any losses.

Complex field of SPPs to the +x-direction a_{x+} and to the −x-direction a_{x-} at the center of the pair can be written as:

$$a_{x+} = \frac{1}{\sqrt{2}}\exp\left(-i\frac{\pi}{4}\right)\sin\left(\frac{\pi}{4}-\psi\right) + \frac{1}{\sqrt{2}}\exp\left(i\frac{\pi}{4}\right)\sin\left(\frac{3\pi}{4}-\psi\right)$$

$$= \frac{1}{\sqrt{2}}\exp(i\psi), \tag{3.1}$$

$$a_{x-} = -\frac{1}{\sqrt{2}}\exp\left(i\frac{\pi}{4}\right)\sin\left(\frac{\pi}{4}-\psi\right) - \frac{1}{\sqrt{2}}\exp\left(-i\frac{\pi}{4}\right)\sin\left(\frac{3\pi}{4}-\psi\right)$$

$$= \frac{1}{\sqrt{2}}\exp\left[i(\pi-\psi)\right], \tag{3.2}$$

where ψ is an orientation angle of the incoming electric field. According to coordinate system, the incoming electric field lies along the x-direction when $\psi = 0$, and along the y-direction when $\psi = \pi / 2$. Multiplied terms of $1/\sqrt{2}$, the exponential function, and the sine function in Equations (3.1) and (3.2) correspond to amplitude projection factor due to tilt angles, phase retardation factor from the spacing between the pair, and amplitude projection factor between the incoming electric field and the nano-aperture, respectively. It is shown that the generated counter-propagating SPPs have the same amplitude

with phase difference of $2\psi - \pi$. If the spacing and tilt angles of the aperture pair array vary, this phase-only modulation of the envelopes cannot be achieved. This result coincides with the previous work done by Lin *et al.* [46], considering that a polarization state of linearly polarized light equals to a linear combination of right-hand and left-hand circular polarizations.
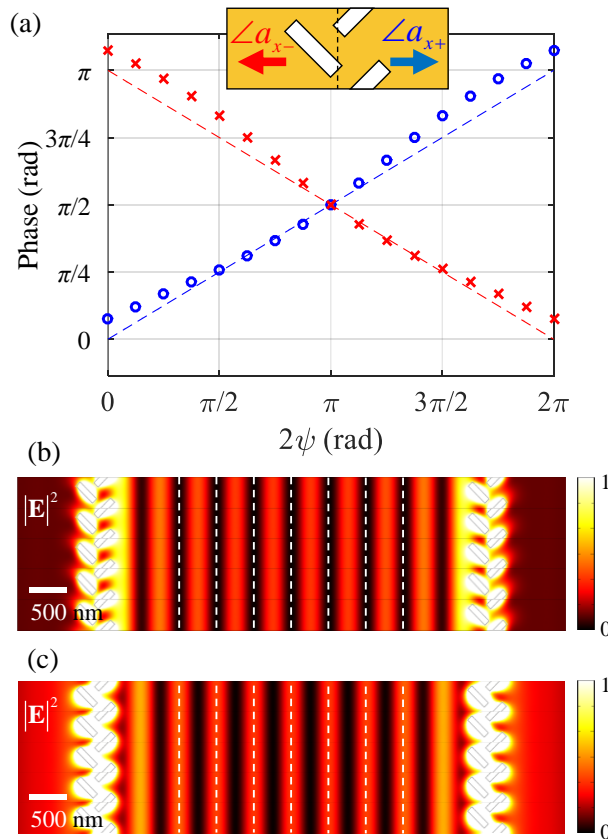
Figure 3.2 (a) Phase of SPP fields generated by the apertures pair array. Normalized electric field intensity profiles of the aperture pair arrays illuminated by the incoming electric field with the orientation angle of (b) 0 and (c) $\pi / 2$.

Phase change of SPPs at a fixed distance with respect to the orientation angle is calculated with the finite element method (FEM) based full-vectorial simulations. Gold film with $t = 300$ nm on a glass substrate is illuminated by the wavelength of 980 nm. Dielectric constants of the gold and glass are − 37.81 + 1.13j and 2.10, respectively [90]. Geometric parameters of the aperture pair array are: $p_x = 240$ nm, $p_y = 400$ nm, $w_a = 80$ nm, and $l_a = 320$ nm. Wavelength of the SPP at the gold-air interface is 967 nm, of which p_x corresponds to about a one-fourth.

Dashed lines in Figure 3.2(a) plot ideal phase profiles according to Equations (3.1) and (3.2). It can be seen that dots, which represent calculated phase, follow the dashed lines. The phase difference between the two SPPs, especially, is almost the same as the analytic results, $2\psi - \pi$. If the two aperture pair arrays are placed with a face-to-face form, interference of counter-propagating SPPs can be controlled by the orientation angle. Figures 3.2(b) and 3.2(c) depict electric field intensity profiles in the xy-plane at 20 nm above the metal surface when the two aperture pair arrays are illuminated by the electric field of $\psi = 0$ and $\psi = \pi / 2$, respectively. Nodes and antinodes between the columns are reversed as the incoming electric field rotates by 90 degrees.

3.3 Design and optimization of a resonator

3.3.1 Control of stored electromagnetic energy using linearly polarized light
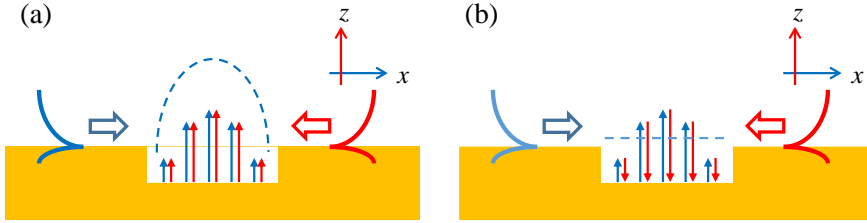
Figure 3.3 Schematic illustrations of (a) the on-state and (b) the off-state controlled by interference between counter-propagating SPPs.

The resonator is made of a rectangular cavity and periodic gratings that act as partial mirrors, so that the quality factor can be increased. As previously explained, counter-propagating SPPs encounter with in-phase at the resonator for $\psi = \pi/2$ case and with out-of-phase for $\psi = 0$ case. That is, averaged electromagnetic energy density $\tilde{u}$ inside the resonator becomes its maximum for the former case, while it becomes the minimum for the latter case. Let the former case *on-state* and the latter case *off-state*. On/off ratio r is defined using $\tilde{u}$ of the two states as:

$$r = \frac{\tilde{u}_{on}}{\tilde{u}_{off}} = \frac{\int_S |\mathbf{E}_{on}|^2 \, dS}{\int_S |\mathbf{E}_{off}|^2 \, dS},$$
(3.3)

where S is the cavity area, and $\mathbf{E}_{on}$, $\mathbf{E}_{off}$ are electric fields of the on-state and the off-state, respectively.

3.3.2 Optimization of a rectangular cavity and periodic gratings
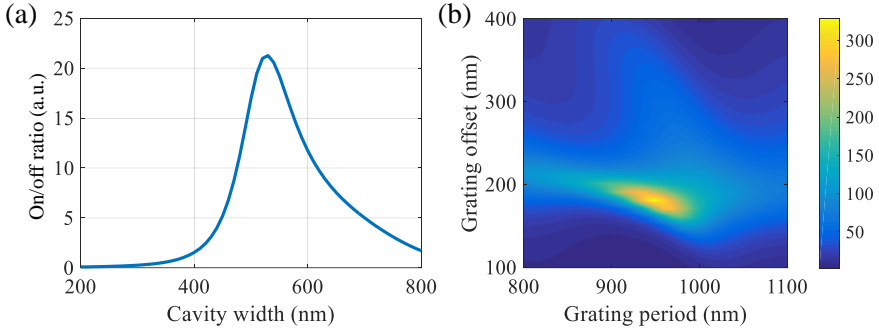
Figure 3.4 (a) The on/off ratio according to the cavity width. (b) The on/off ratio map with respect to the grating period and offset.

In order to optimize the resonator, geometric parameters are investigated. At first, w_c, width of the cavity, is examined. It is shown in Figure 3.4(a) that the first order resonance occurs when w_c is around a half of the SPP wavelength. The maximum on/off ratio is achieved as 20.1, with the width of 520 nm. Then, the grating period and the offset, which is a distance between the edge of the cavity and the first grating, are inspected since they also have periodicity related with the wavelength. The on/off ratio map according to each parameter is depicted in Figure 3.4(b). Other auxiliary parameters are set as $d_c = 200$ nm, $d_g = 110$ nm, and $w_g = 80$ nm. The optimum condition appears when p_g is about a wavelength of the SPP. The on/off ratio increases about 15 times, compared with the on/off ratio without the gratings. It

27

indicates that the gratings play a role of amplifying the resonance. The grating period is determined as 940 nm and the offset as 180 nm. The *Q*-factor of the optimized resonator is 81.4.
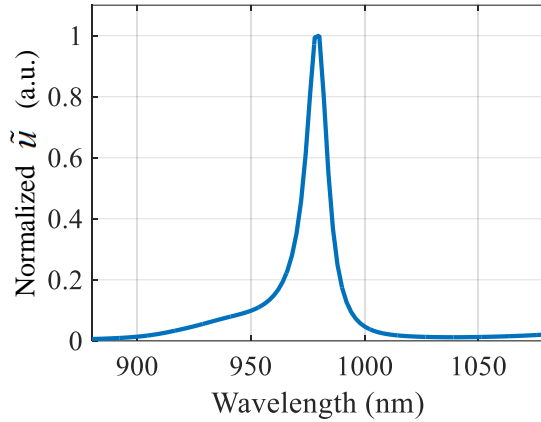
Figure 3.5 Spectrum of stored electromagnetic energy inside the cavity.

Figure 3.6 shows simulation results of the overall device, including the aperture pair arrays and the resonator. The averaged energy density inside the cavity, which is normalized by that of the off-state, rises from 1 to 430 as ψ changes from 0 to $\pi / 2$. As well as the energy density of the on-state and the off-state, an intermediate amount of the energy density can be obtained by the appropriate orientation angle that agrees with the relation of Figure 3.6(a). Cross-sectional electric field intensity profiles in Figures 3.6(b) and (c) clearly show the result. Strong electric fields appear at the cavity for the on-state, while electric fields are enhanced at the gratings rather than the cavity for the off-state.

(a)

(b)

(c)
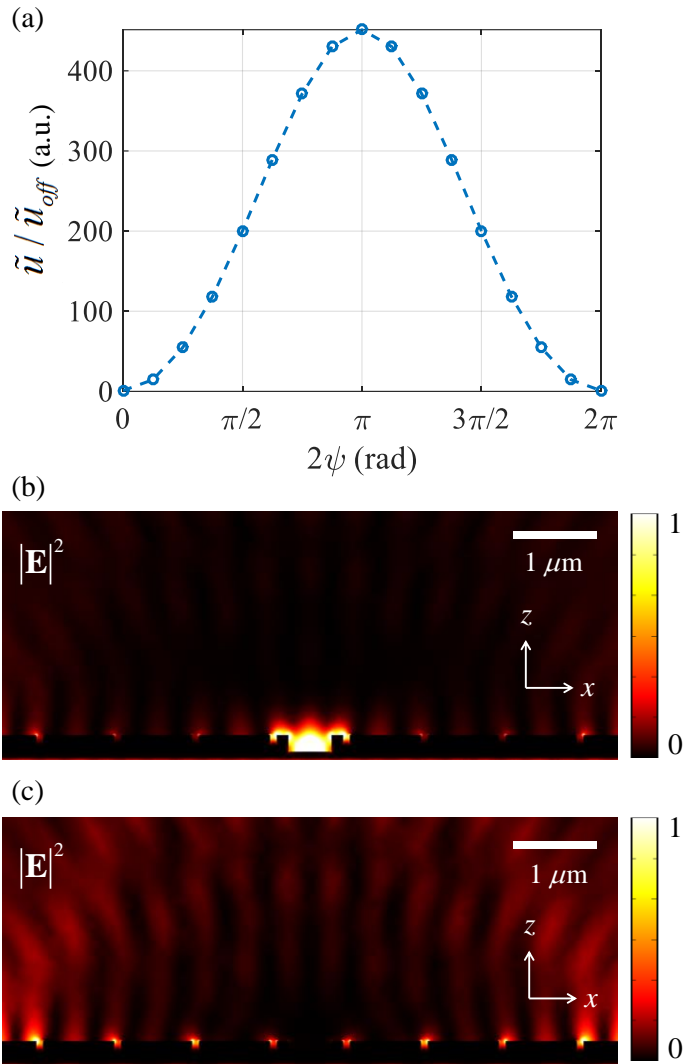
Figure 3.6 (a) Averaged energy density inside the cavity normalized by that of the off-state with respect to the orientation angle. Cross-sectional normalized electric field intensity profiles of (b) the on-state and (c) the off-state.

3.4 Experimental demonstration
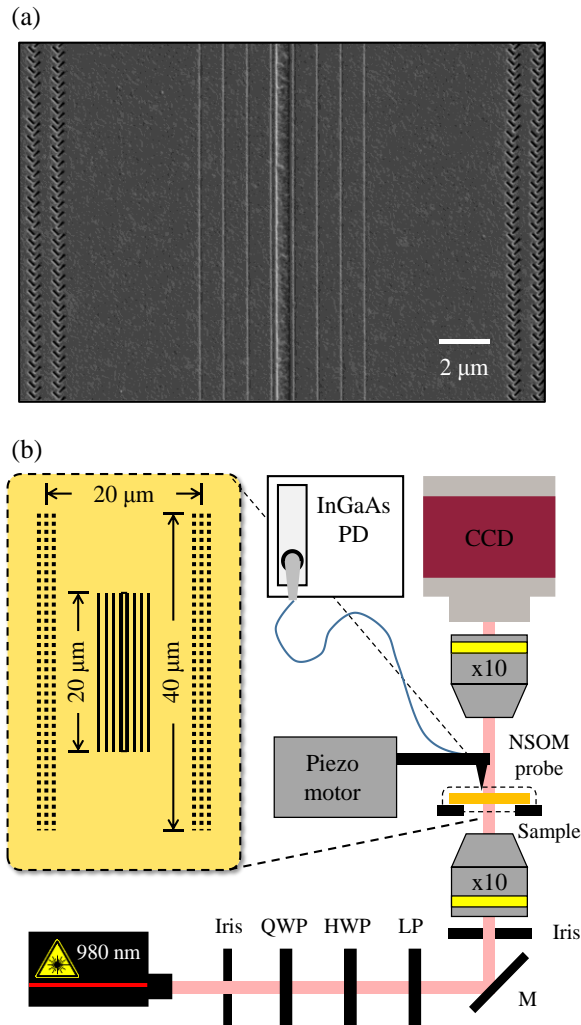
Figure 3.7 (a) SEM image of the fabricated sample. (b) Experimental apparatus measuring the near-field images. M: mirror, QWP: quarter-wave plate, HWP: half-wave plate, LP: linear polarizer, CCD: charge-coupled device, PD: photodetector, and x10: objective lens of x10.

The optimized device is fabricated on a gold film using the focused ion beam (FIB) milling with source voltage of 30 kV and current of 1 pA (FEI, Helios 650). The aperture pair arrays of 3 periods along the *x*-direction and 100 periods along the *y*-direction are perforated on a 300-nm-thick gold film deposited on a 1 mm thick piecewise slide glass (Marienfeld, plain) by e-beam evaporator (KVT, KVE-3004). Periodic arrangement of the array along the *x*-axis, with the period equal to the SPP wavelength, is placed to enhance SPP signal levels. After that, the gratings and the cavity are positioned at the center of the face-to-face aperture pair arrays. A SEM image of the fabricated sample is shown in Figure 3.7(a).

Experimental setup is illustrated in Figure 3.7(b). Near-field images are measured using NSOM (Nanonics, MultiView 4000) with an aperture probe with 250 nm core diameter. Optical power though a fiber from the probe is detected by an InGaAs photodetector (Agilent, 81634B). The sample is illuminated by the laser of 980 nm wavelength after passing a set of the wave plates and the polarizer, which renders light into linear polarization states. The orientation angle is changed by rotating the polarizer. It is worth to note that near-field imaging based on raster scanning is inadequate to measure interferometry in general because it is vulnerable to vibrational noise during the measurement. According to the experimental scheme in Figure 3.7(b), however, noise in the optical path affects the same for the both path lengths, so that disturbance can be cancelled out. This makes the imaging more impervious to vibrational noise.

Near-field images with scanning window of 33 μm × 33 μm at the on-state and the off-state are depicted in Figure 3.8. It is shown that bright

double lines appear at the cavity of the on-state. Because of low signal level of the off-state, the near-field profile is detected with more noises that result in diagonal stripes in Figure 3.8 (b).

(a)

(b)
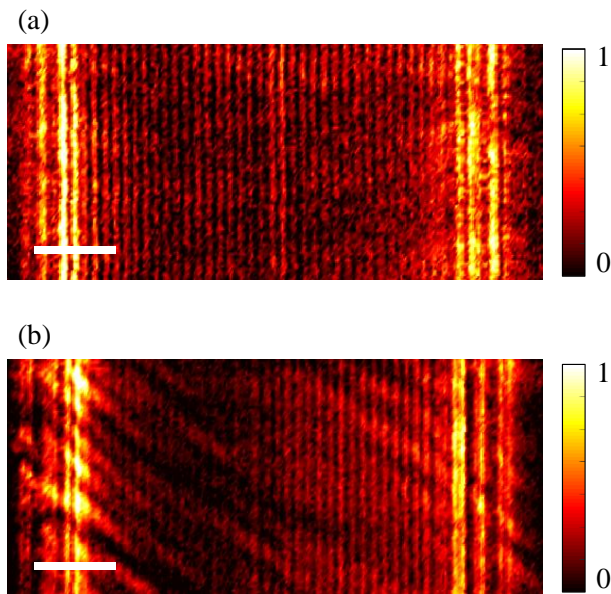
Figure 3.8 NSOM images at (a) the on-state and (b) the off-state. Scale bars represent 5 μm.

For the sake of precise comparison between the field profiles, magnified NSOM images are acquired by narrowing scanning window to 14.5 μm × 14.5 μm around the center. The exact position of the cavity is obtained by analyzing surface morphology data collected from an auxiliary atomic force microscopy (AFM) probe of the NSOM system. Figure 3.9 shows raw data acquired from the NSOM and AFM probes. Positions of the cavity and the gratings are clearly recognized. Measured NSOM data are then averaged along the y-axis in order to clarity the signals. The y-axis is also specified by the surface morphology data, which is normal to the orientation of the cavity.
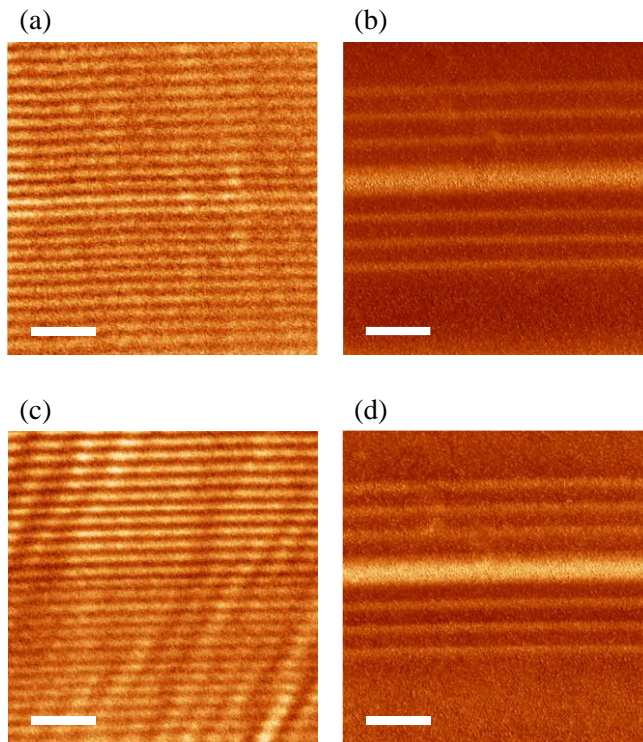
Figure 3.9 Raw NSOM data and corresponding auxiliary AFM data at (a, b) the on-state and (c, d) the off-state. Scale bars represent 3 μm.
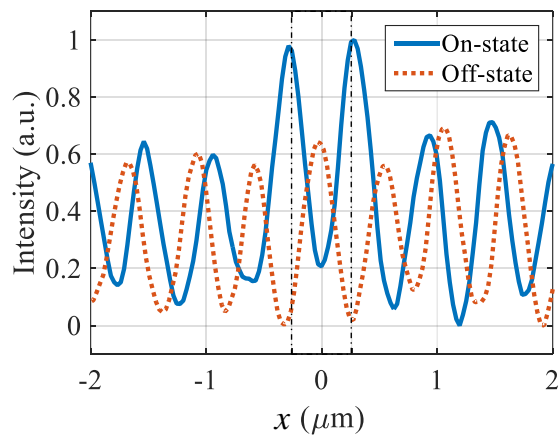
Figure 3.10 Cross-sectional intensity profiles near the cavity. Dash-dotted line corresponds to the cavity.

Figure 3.10 plots cross-sectional intensity near the center of the sample. As well as shifting of nodes and antinodes, near-field intensity of the on-state is seized strongly at the edge of the cavity, whose width is lined with dash-dot in Figure 3.10. This result seems different from the energy density profile depicted in Figure 3.6(b), however, since the energy density is enhanced markedly at the center of the cavity rather than the edges. This difference can be explained by uneven coupling efficiency between each electric field component and the NSOM probe. Properties of the NSOM probe, such as aperture type, core diameter, and tilt angle can influence the coupling efficiencies among the field components [98]. Especially for the proposed resonator, amount of the in-plane electric fields (E_x-field) and the electric fields normal to the surface (E_z-field) are almost leveled inside and near the cavity. Thus, the uneven coupling efficiencies can make intensity profiles different from the exact energy density profiles.

Based on the cross-sectional intensity profiles, the on/off ratio is figured out. As previously mentioned, measured near-field intensities have some discrepancies from the exact energy density. That is, the on/off ratio cannot be computed as the same way that is applied for simulation results. Instead, the maximum intensity values inside the cavity of each state are adopted, noticing that ratios of the maximum values are similar among the field components. The final on/off ratio is found out as 1.55.

The on/off ratio derived from the experimental results, however, is not as remarkable as that from the simulation results. The major drawback is fabrication errors of the resonator. For example, due to sensitive resonant condition with high Q-factor, 20 nm difference of the cavity width from the

34

target dimension decreases the on/off ratio down to one-tenth of the optimum value. Geometric defects of the resonator, rough surface morphology of the bottom of the cavity, tapered sidewalls, and fillets at the grating edges for examples, also contribute to reduce Q-factor of the resonator. With regard to the measurement system, laser source with higher output power can improve clarity of the images by increasing the signal-to-noise ratio of measured near-field intensities. Furthermore, other imaging techniques that are able to collect optical power directly proportional to energy density inside the cavity can help to improve the measurement, for instance fluorescence imaging using deposition of dye molecules and quantum dots [99–101].

3.5 Summary and discussions

A plasmonic resonator is designed and demonstrated whose electromagnetic energy density can be controlled by the orientation angle of the incident electric field. Interferometric control of SPPs, which are excited by the nano-aperture pairs, makes the resonator tunable. After optimizing the resonator, the on/off ratio reaches 430. This large tunability can be utilized in optical transceivers and particle trapping systems. Near-field images are measured using NSOM by actuating only the angle of the polarizer. Based on the working principle of our work, interferometric control is possible without exquisite alignment of optical path length. That is, experimental setup of the interferometry can be significantly simplified. The proposed method can contribute to realizing all-optically controlled active plasmonic devices and coherent network elements, and developing more compact polarization-sensitive optical systems.

In this chapter, interferometric control of SPPs are discussed based on linear polarization states. The helicity information of light, however, is discarded. It will be investigated to make use of both an orientation and an ellipticity angle of a polarization state in the following chapters.

Chapter 4 Directional launching and switching of SPPs using elliptically polarized light

4.1 Introduction

Here, directional launching and switching of SPPs using elliptically polarized light are proposed based on a hybrid aperture pair array. The hybrid aperture pair is composed of two rectangular aperture pairs with different size factor. Due to different coupling coefficient between SPPs generated by each aperture pair, SPPs propagate to a single direction at the given elliptically polarize light. Starting from an analytic model that deals with SPPs generated by a simple complex field with uniform wavefront, numerical and experimental verifications are presented.

4.2 Principles of hybrid aperture pair array

4.2.1 Configuration of a hybrid aperture pair
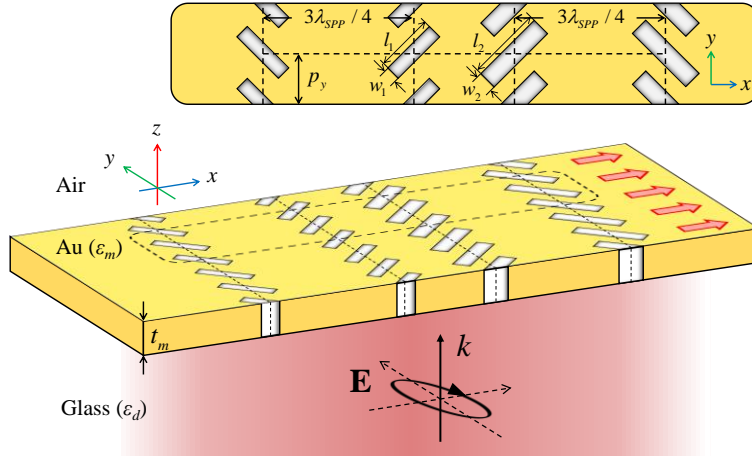
Figure 4.1 Directional launching scheme of SPPs using array of hybrid aperture pairs and elliptically polarized light. Inset shows top-view of the hybrid aperture pairs.

In Section 2.2.2, excitation of SPPs through a single column and double columns of the aperture array is explained. The double columns of the aperture array act as a polarized beam splitter that splits SPPs into the RCP component and the LCP component. However, polarized beam splitting according to the helicity of the incoming light abandons information about an orientation angle of the polarization since field intensities of propagating SPPs to each x-direction are determined by the distance between the columns and the helicity of the input beam. If splitting of SPPs that is sensitive to both the orientation angle and the helicity of the incident light is possible,

controllability coverage can be extended to the entire surface of the Poincaré sphere, not only the polar points.

Here, additional double columns of the aperture array are introduced as shown in Figure 4.1. The aperture array columns are composed of two sets of aperture pairs, which are coined as a *hybrid aperture pair*. Let the two aperture columns at the left side be *Pair 1*, and the right side be *Pair 2*. Pair 1 and 2 have the same period along the *y*-direction and the distance between the adjacent columns is $3\lambda_{SPP} / 4$. Both Pair 1 and 2 operate as polarized beam splitters. However, their tilt angles are allocated inversely, $(-\pi/4, \pi/4)$ for Pair 1 and $(\pi/4, -\pi/4)$ for Pair 2. Hence, splitting directions with respect to the helicity of the incident light are opposite to each other, between Pair 1 and 2. In addition, coupling efficiencies of each pair to SPPs are different due to variation of lengths and widths.

Consider the case of the RCP illumination at Pair 1 and Pair 2. Electric field profile of the incident light is:

$$\mathbf{E}_{in} = \frac{E_0}{\sqrt{2}}(1, -j, 0)e^{jk_s z}, \qquad (4.1)$$

where k_s is wavenumber of the dielectric substrate. As shown in Figure 2.6(b), SPPs generated by Pair 1 will propagate to the –*x*-direction. According to Equation (2.2), E_z-field of the propagating SPP mode can be written by:

$$E_{z,x-} = E_{SPP1}e^{-jk_{SPP}x}e^{-\kappa_d z}. \qquad (4.2)$$

Neglecting an intrinsic loss of SPPs, a coupling coefficient of SPPs generated by Pair 1 is then defined by a ratio between complex amplitudes of the incident field and the E_z-field of SPPs:

$$c_1 = \frac{E_{\text{SPP1}}}{E_0}.\tag{4.3}$$

In a similar way, the coupling coefficient by Pair 2 can be obtained. In a case of Figure 4.2 (b), $|c_1| < |c_2|$ since Pair 2 has large footprint.

Size factor of the hybrid aperture pair can be then fully characterized by a coupling ratio c and phase difference δ as:

$$c = \left|\frac{c_1}{c_2}\right|,\tag{4.4}$$

$$\delta = \angle c_2 - \angle c_1,\tag{4.5}$$

where $\angle$ is an argument function of a complex number.

Suppose that elliptically polarized light with an orientation angle ψ and axial lengths of a and b as Figure 4.2(a) illuminates Pair 1 and 2. Right-hand rotated field is assumed in this case. Each CP component in the elliptical polarization can be obtained from the Jones calculus as:

$$\mathbf{J} = \begin{pmatrix} a\cos\psi + jb\sin\psi \\ a\sin\psi - jb\cos\psi \end{pmatrix} = \frac{a+b}{\sqrt{2}}e^{j\psi}\mathbf{J}_\mathrm{R} + \frac{a-b}{\sqrt{2}}e^{-j\psi}\mathbf{J}_\mathrm{L}, \quad (4.6)$$

where ψ is an orientation angle of the polarization ellipse and the Jones vectors $\mathbf{J}_\mathrm{R} = 1/\sqrt{2}\,(1, -j)^\mathrm{T}$ and $\mathbf{J}_\mathrm{L} = 1/\sqrt{2}\,(1, j)^\mathrm{T}$ denote SOPs of the RCP and LCP, respectively. Exchange of the sign of b can describe the field incidence of left-hand rotation. Derived relation shows that the RCP and the LCP component have amplitude ratio of $(a + b) : (a - b)$ with phase difference of 2ψ.
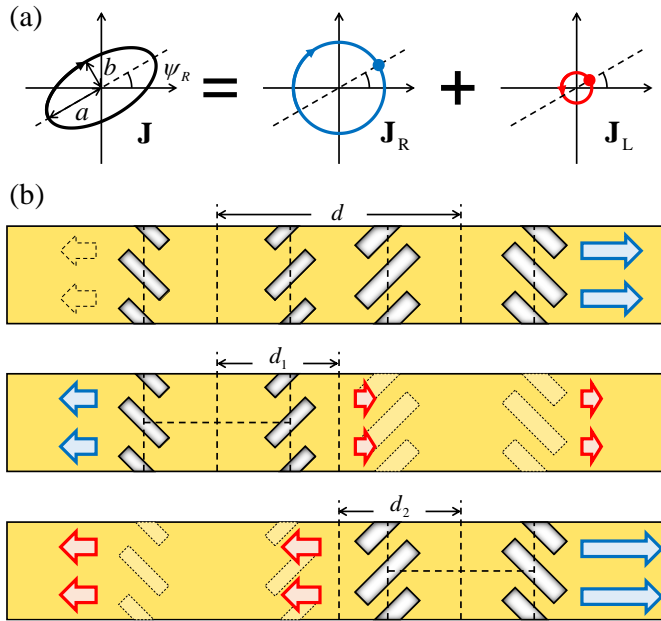
Figure 4.2 (a) Polarization ellipse denoting the SOP of the illuminated beam. (b) Working principle of a hybrid aperture pair array with component-wise picture of Pair 1 (middle) and Pair 2 (bottom).

As mentioned above, Pair 1 and 2 split the RCP and LCP component of the incident light to opposite direction of SPPs. As shown in Figure 4.2(b), Pair 1 (middle) releases the RCP component of the incoming light to the $-x$-direction of SPPs (blue arrows), while the LCP component to the $+x$-direction (red arrows). For the case of Pair 2, SPPs couple in the opposite manner. Size of each arrow illustrates magnitude of coupled SPPs by the pairs schematically. Net SPPs to each x-direction can be obtained by superposition of two cases, as seen in the top of Figure 4.2(b). If it is possible to match the blue arrows of Pair 1 and the red arrows of Pair 2 with the same magnitude but phase difference of π, SPPs to the $-x$-direction will be canceled out. Therefore, SPPs will propagate only to the $+x$-direction. Such matching condition can be found by investigating relation among coupling coefficients c_1, c_2, and the RCP/LCP components derived from Equation (4.6). At first, amplitude of SPPs excited by Pair 1 and Pair 2 should be the same. The coupling ratio c satisfies

$$c_0 = \frac{a+b}{a-b}. \tag{4.7}$$

The subscript 0 denotes the matched condition that SPPs from Pair 1 and 2 are canceled out. Here, intrinsic loss of SPPs and secondary scattering that occurs when coupled SPPs cross over the other apertures are neglected to simplify an analytic model.

Secondly, consider phase terms of SPP complex fields. The phase term includes geometric phase from each polarization component, retarded phase

due to traveling of SPPs, and phase difference δ due to the size factor of the aperture. The phase term of SPPs to the $-x$-direction excited by Pair 1, φ_1, can be written as:

$$\varphi_1 = \psi - k_{\mathrm{SPP}}d_1 + \delta_1, \tag{4.8}$$

where k_{SPP} is a wavenumber of the SPP. Similarly, the phase term of SPPs by Pair 2 is:

$$\varphi_2 = -\psi + k_{\mathrm{SPP}}d_2 + \delta_2. \tag{4.9}$$

Then the phase difference δ is achieved from the total phase difference $\varphi_2 - \varphi_1$ at the out-of-phase condition as:

$$\delta_0 = 2\psi - k_{\mathrm{SPP}}d + (2n-1)\pi, \tag{4.10}$$

where n is an integer number. For the LCP-dominant incident field, signs of the geometric phase term and the retarded phase term are switched as:

$$\delta_0^c = -2\psi^c + k_{\mathrm{SPP}}d + (2m-1)\pi. \tag{4.11}$$

This implies that there is a conjugate polarization state $\mathbf{s}_0^c$ of $\mathbf{s}_0$ that can excite SPPs to the other direction.

In summary, it is possible to generate SPPs to a single direction for the given arbitrary SOP $\mathbf{s}_0$, by properly designed hybrid aperture pair array with the size factor satisfying c_0 and δ_0. In addition, propagating direction of SPPs can be switched by the conjugate polarization state $\mathbf{s}^c$.

In reverse, $\mathbf{s}_0$ can be found at the given hybrid aperture pair. An ellipticity angle χ_0 of the polarization ellipse is directly obtained from the coupling ratio c from Equations (4.4) and (4.7) and the definition of the ellipticity angle as:

$$\chi_0 = \arctan\left(\frac{c-1}{c+1}\right). \tag{4.12}$$

The orientation angle ψ is affected by two parameters of d and δ. According to Equations (4.10) and (4.11), ψ_0 and its conjugate ψ_0^c can be rewritten as:

$$\psi_0 = (2n-1)\frac{\pi}{2} + \frac{k_{\mathrm{SPP}}d}{2} + \frac{\delta}{2}, \tag{4.13}$$

$$\psi_0^c = (2m-1)\frac{\pi}{2} + \frac{k_{\mathrm{SPP}}d}{2} - \frac{\delta}{2}. \tag{4.14}$$

Derived equations show relation among ψ_0, ψ_0^c, d, and δ explicitly. Both orientation angles vary the same amount with respect to the change of d. On the other hand, deviation between ψ_0 and ψ_0^c increases when δ increases.

Hence, an arbitrary set of ψ_0 and $\psi_0{}^c$ can be attained by engineering d and δ.

4.2.2 Design of hybrid aperture pairs and examples
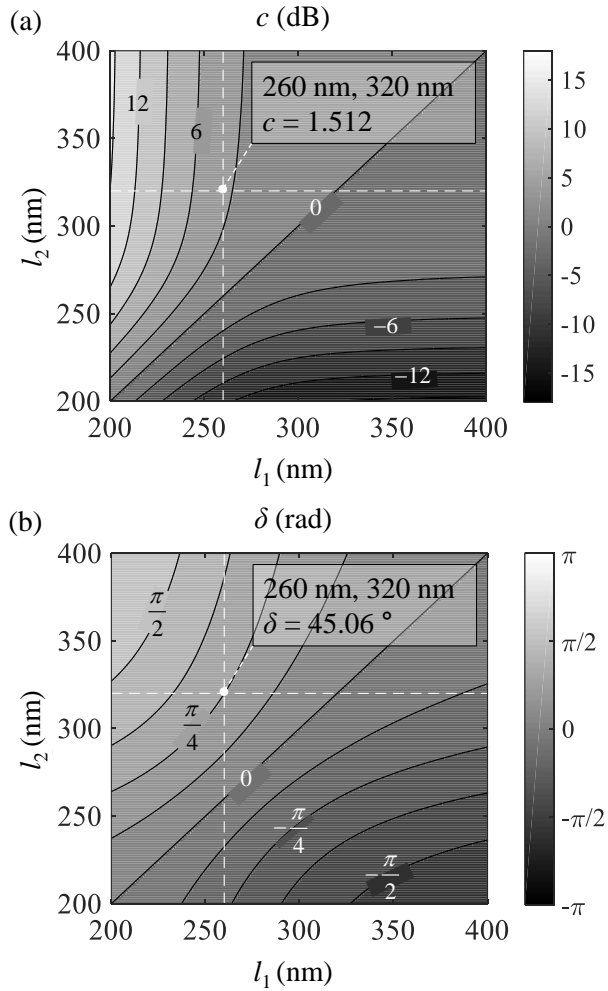
Figure 4.3 Contour maps of (a) the coupling coefficient c and (b) the phase difference δ according to length of the rectangular apertures.

Figure 4.3 shows contours of c and δ based on the array of single aperture pair (see Figure 2.6) perforated on a 200 nm thick gold film. The coupling coefficient c is presented in dimension of dB to show the result more clearly. l_1 and l_2 denote length of each pair. Width is fixed as a quarter of the length. FEM is used for the calculation with following parameters: wavelength $\lambda_0 = 980$ nm, distance between the face-to-face aperture columns $3\lambda_{SPP} / 4 = 720$ nm, period along the y-direction $p_y = 240$ nm, dielectric constant of the gold film $\varepsilon_{Au} = -37.81 + j1.13$ [90], and refractive index of a substrate 1.45. c and δ are obtained from near-field components delivered by SPPs when the aperture pair array is illuminated by the RCP. Thickness of the gold film and range of the aperture length are selected considering wavelength of the incident field, to avoid abrupt change of the coupling ratio c and the phase difference δ due to resonance rising at a single aperture.

Each point in Figures 4.3(a) and (b) indicates c and δ of the hybrid aperture where the lengths of each pair are given by l_1 and l_2, respectively. For instance, Pair 1 of 260 nm and Pair 2 of 320 nm length give $c = 1.512$ and $\delta = \pi / 4$. The hybrid aperture with Pair 1 of 210 nm and Pair 2 of 340 nm have $c = 4.441$ and $\delta = \pi / 2$. In order to verify the proposed model, a case of $c = 1.512$ and $\delta = \pi / 4$ is chosen, which is mentioned at the previous example. According to Equations (4.12), (4.13), and (4.14), deviation of the orientation angle $\psi_0 - \psi_0^c$ will be $\pi / 4$ and the ellipticity angle χ_0 be 11.5 °. Length and width of Pair 1 are selected as 260 nm and 70 nm, respectively, and 340 nm and 75 nm for Pair 2 after additional slight tuning of lengths and widths. If SPPs excited by the hybrid aperture are the exact superposition of Pair 1 and Pair 2, intensities of SPPs propagating to the $+x$-direction I_{x+} and

the −x-direction I_{x-} at the polarization angles of ψ and χ will be expressed using Equations (4.6), (4.10) and (4.11) as:

$$I_{x+} = I_0 \left[c_0^2 a_R^2 + a_L^2 + 2c_0 a_R a_L \cos\left(2\psi - k_{SPP}d + \delta_0\right) \right], \quad (4.15)$$

$$I_{x-} = I_0 \left[a_R^2 + c_0^2 a_L^2 + 2c_0 a_R a_L \cos\left(2\psi - k_{SPP}d - \delta_0\right) \right], \quad (4.16)$$

where $a_R = \sin^2\left(\chi + \pi/4\right)$ and $a_L = \sin^2\left(\chi + 3\pi/4\right)$. Extinction ratio is then defined by a ratio between two intensities,

$$r \, [\text{dB}] = 10\log_{10}\left(\frac{I_{x+}}{I_{x-}}\right). \quad (4.17)$$

Figure 4.4 shows extinction ratio in the case of $d = 1440$ nm. The polarization angles at directional launching of SPPs are obtained by $(\psi_0, \chi_0) = (22.5\,°, 11.5\,°)$ and $(\psi_0^c, \chi_0^c) = (157.5\,°, −11.5\,°)$, which are black dashed lines and white dashed lines respective in Figures 4.4(b) and (c). Figure 4.4 (b) depicts analytic results according to Equations (4.16) and (4.17), while Figure 4.4(c) is the result using the FEM simulation with the geometry in Figure 4.4(a). It is shown that the hybrid aperture pair array operates as expected by comparing Figures 3.4(b) and (c).
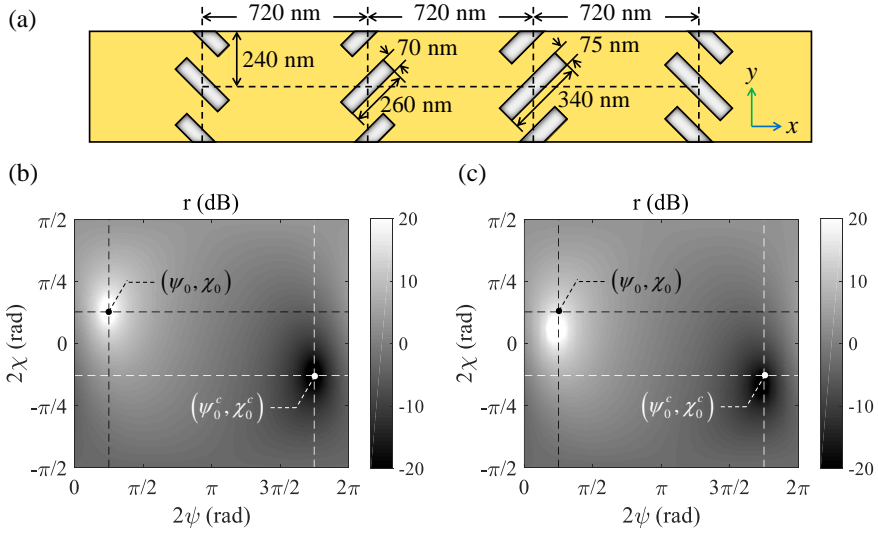
Figure 4.4 (a) The hybrid aperture pair array with $d = 1440$ nm. (b) Extinction ratio computed by analytic model according to Equations (4.15) and (4.16). (c) Extinction ratio calculated by the FEM.
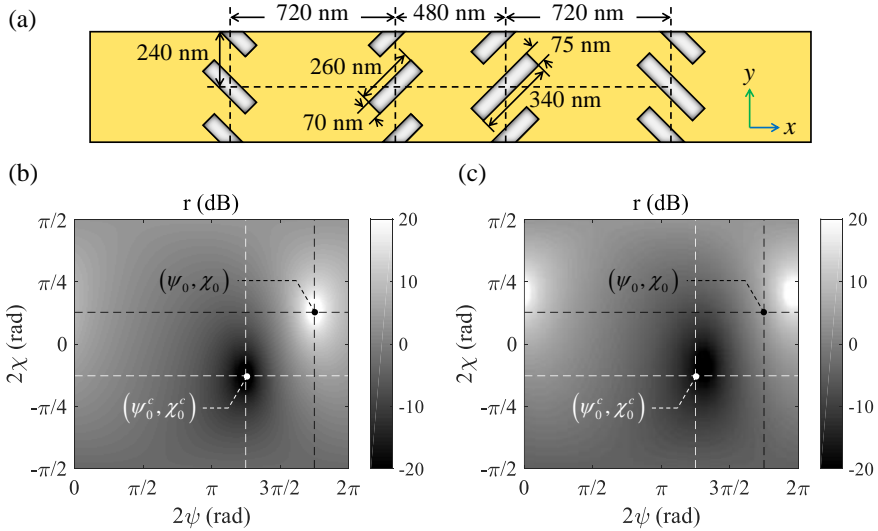
Figure 4.5 (a) The hybrid aperture pair array with $d = 1200$ nm. (b) Extinction ratio computed by analytic model according to Equations (4.15) and (4.16). (c) Extinction ratio calculated by the FEM.

Figure 4.5 is another example, which is introduced to check validity of Equations (4.13) and (4.14). The second type of the hybrid aperture pair array has the same geometric parameters with the first one, except for d. In this case, d is 240 nm shorter than the previous case, which is equivalent to a quarter of the SPP wavelength. Because the size factor is the same, χ at the directional launching condition is the same with the previous example. On the other hand, ψ rotates $-\pi/4$ due to the change of d. Therefore, the polarization angles will be $(\psi_0, \chi_0) = (157.5\degree, 11.5\degree)$ and $(\psi_0{}^c, \chi_0{}^c) = (112.5\degree, -11.5\degree)$. The simulation result of the second example also follows the analytic result, but some amount of deviation at (ψ_0, χ_0). The deviation implies c and δ of Pair 1 and 2 differ according to the helicity of the incoming light. Considering that the change of the helicity is equivalent to switch of the coordinate from $+x$ to $-x$ or from $+y$ to $-y$, it can be said that this asymmetry is inherited from the geometrical asymmetry of the hybrid aperture array. The hybrid aperture array does not have even geometry with respect to the x-axis nor the y-axis. For example, SPPs excited by Pair 1 traveling to the $+x$-direction encounter Pair 2, while those to the $-x$-direction glide without bumping to any additional scatterers. This issue can be handled if Pair 1 and 2 are overlapped so that the geometry gets symmetry. The overlapped hybrid aperture array, or an X-shaped aperture array will be introduced and discussed in Chapter 5.
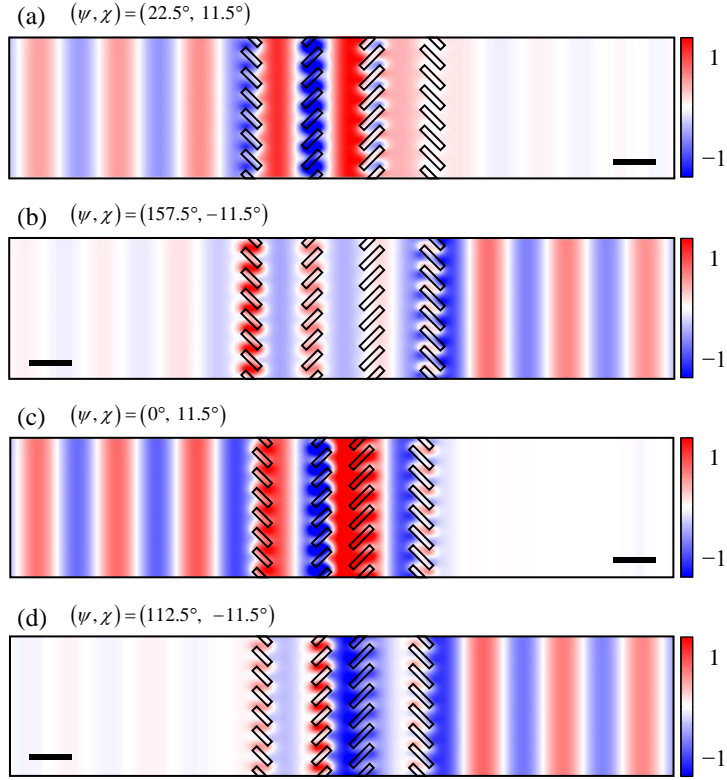
Figure 4.6. H$_y$-field profiles of SPPs at (a, b) the case of $d = 1440$ nm and the case of $d = 1200$ nm. Scale bar indicates 500 nm.

Figure 4.6 depicts SPPs at each directional launching condition for the two examples. H$_y$-field profiles in the xy-plane at 20 nm above the metal surface are plotted in order to clearly show near-fields carried by SPPs. All the fields are normalized with the same scale. It is seen that SPPs travel to the single direction with uniform wavefront. Extinction ratios are 16.9 dB, −19.2 dB, 18.3 dB, and −24.1 dB, from Figures 4.6(a) to (d), respectively.

4.3 Experimental demonstration

4.3.1 Fabrication and measurement setup
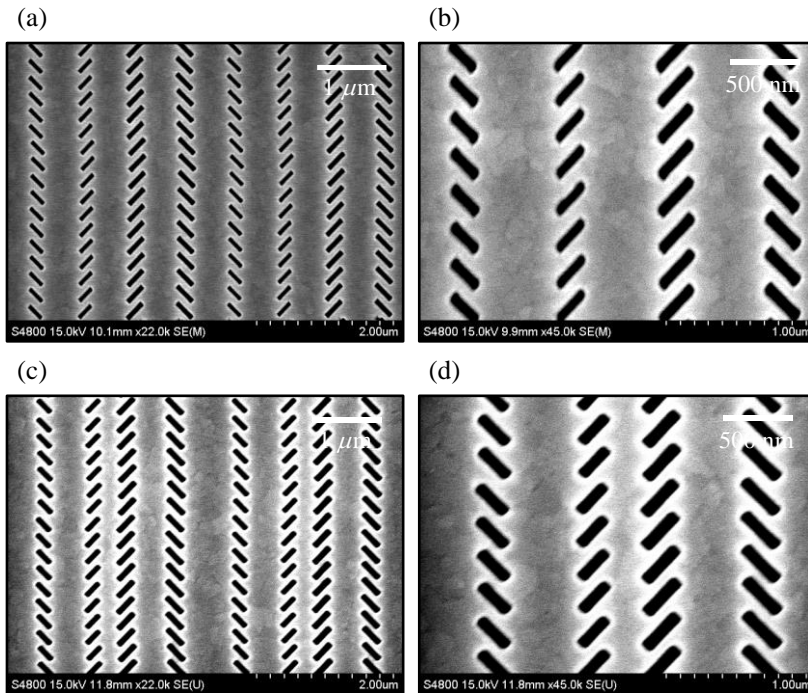
Figure 4.7 SEM images of (a, b) the hybrid aperture arrays with $d = 1440$ nm, (c, d) $d = 1200$ nm, and (e, f) an outcoupler

Focused ion beam (FEI, Quanta 200 3D) milling is used for fabrication of the hybrid aperture array with the geometries of Figures 4.4(a) and 4.5(a). Hybrid aperture pair arrays of 2 periods along the x-direction and 100 periods along the y-direction are perforated on a 200 nm thick gold film deposited on a 1 mm thick piecewise slide glass (Marienfeld, plain) by e-

beam evaporator (KVT, KVE-3004). Twenty periods of the array are engraved at a single exposure of FIB with 10 pA of current and 30 kV of source voltage. The same exposure is repeated 5 times after translating the sample holder by 4.8 μm along the *y*-axis between the each step. Milling sequence is allocated row-by-row following a zigzag manner in order to locate each aperture at a precise position. Figure 4.7 shows SEM images (Hitachi, S-4800) of fabricated hybrid aperture arrays. Lengths, widths, and distances among adjacent apertures are matched to the target parameters after several times of adjustments.
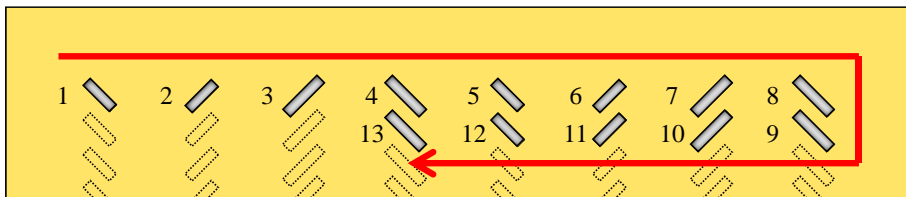
Figure 4.8 Schematic illustration of FIB milling sequence.

In order to measure optical near-fields of SPPs, outcouplers are positioned at the equal distance, 30 μm, from the hybrid aperture array. The outcoupler is a periodic grating that radiates incoming SPPs to the free space as illustrated in Figure 4.9(a). Optical power delivered by SPPs to each direction can be compared by measuring brightness of each outcoupler by the CCD. The outcoupler is fabricated to have 880 nm period with 0.5 fill factor, 5 periods, 80 nm depth, and 18 μm length. The distance between the outcouplers is preferred to be closer to the hybrid aperture array considering a coupling efficiency. However, if the distance between the outcouplers are

too close, parasitic interference due to reflected SPPs at the outcoupler can disturb the result. The distance of 30 μm is set to compromise these two issues after several times of experimental trials. The period is determined to have the highest coupling efficiency based on numerical studies.
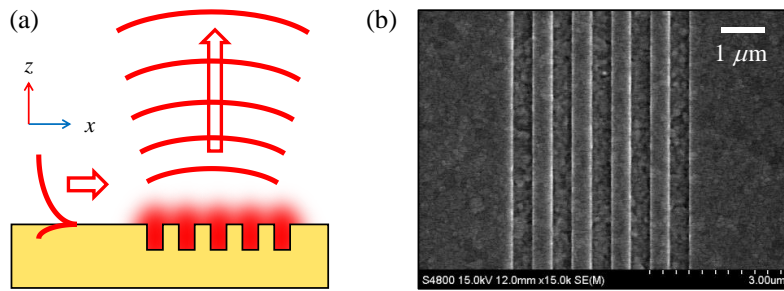
Figure 4.9 (a) Operation mechanism of an outcoupler and (b) a SEM image of fabricated outcoupler.

Experiment apparatus is setup based on continuous wave laser of 980 nm wavelength as shown in Figure 4.10. Output power of the laser beam is about 200 mW. A set of a polarizer and wave plates are placed to produce arbitrary elliptically polarized light. Two former wave plates are fixed to produce circular polarization that makes the illuminated power constant regardless of the polarization state after the linear polarizer. The linear polarizer and the half-wave plate synthesize desired SOPs by rotating to appropriate angles after that. All optical elements on a path including mirrors are anti-reflection coated with operating wavelengths from 700 nm to 1100 nm. The fabricated sample on a stage is illuminated from the backside by a normally incident laser beam that covers the whole area of the sample

uniformly. At the frontside of the sample, a CCD camera captures images magnified by an x 50 objective lens (Allied Vision, Mako G-223). Position of a mirror below the stage is toggled in order to obtain the images of the illuminated sample and the incident polarization simultaneously. A commercial polarimeter is used to detect SOPs of the laser beam after the polarizer and wave plates (Thorlabs, PAX5710IR-T).
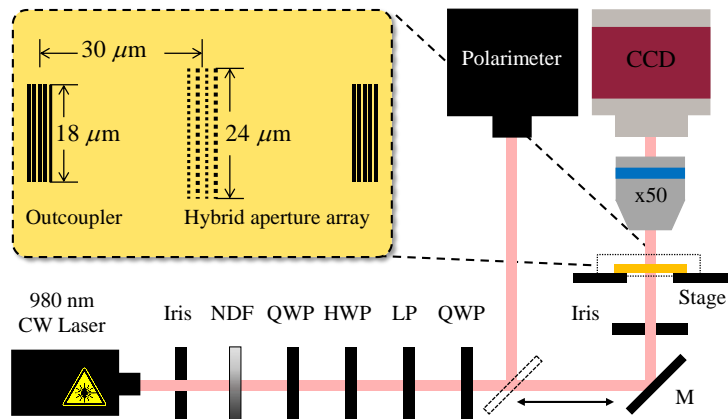
Figure 4.10 Schematic illustration of measurement setup. Inset illustrates a top-view of the sample. M: mirror, NDF: neutral-density filter, QWP: quarter-wave plate, HWP: half-wave plate, LP: linear polarizer, CCD: charge-coupled device, and x50: objective lens of x 50.

4.3.2 Measured extinction ratios

Captured images of the hybrid apertures at given SOPs are shown in Figures 4.11 and 4.12. Bright areas at the center correspond to the transmitted light through the hybrid aperture pair arrays. The outcouplers are located at the both ends of presented images. It can be seen that brightness of each outcoupler changes according to polarization states of the incident light. It is worthy of noting that the outcouplers are thoroughly turned off at the left-most case in Figure 4.11(a) and the right-most case in Figure 4.11(b). This implies that radiated fields at the outcouplers only depend on excited SPPs, without permitting any direct transmission of the incident light.

For the sake of comparison, calculated field profiles, which show normalized electric field intensities $|\mathbf{E}|^2$ 100 nm above the surface, are presented below the corresponding captured images. Here, a numerical model that assumes anisotropic subwavelength apertures as dipole sources is used (see Ref. [55] for more detailed descriptions). The calculated profiles directly depict near-field intensities delivered by SPPs generated by the hybrid aperture pair array. Similarly, the aperture arrays are located at the center of the figures. It can be seen that intensities at the right and the left side of the aperture arrays change according to the given polarization states. Noting that there is a linear relation between intensities of SPPs and intensities of radiated fields by the outcouplers, captured images and corresponding calculated field profiles show close proximity to each other.

(a) $\chi = 11.3\,°$

$\psi = 26.0\,°$　　　　$\psi = 71.0\,°$　　　　$\psi = 116.0\,°$　　　　$\psi = 161.0\,°$

(b) $\chi = -11.3\,°$

$\psi = 26.0\,°$　　　　$\psi = 71.0\,°$　　　　$\psi = 116.0\,°$　　　　$\psi = 161.0\,°$
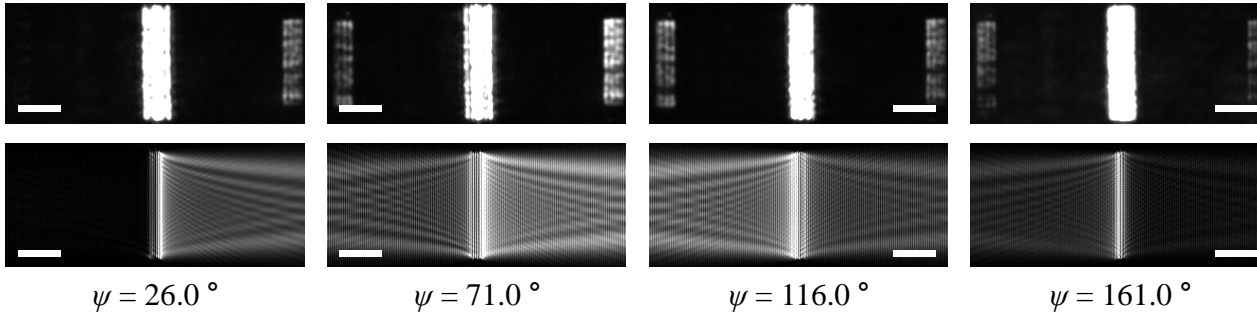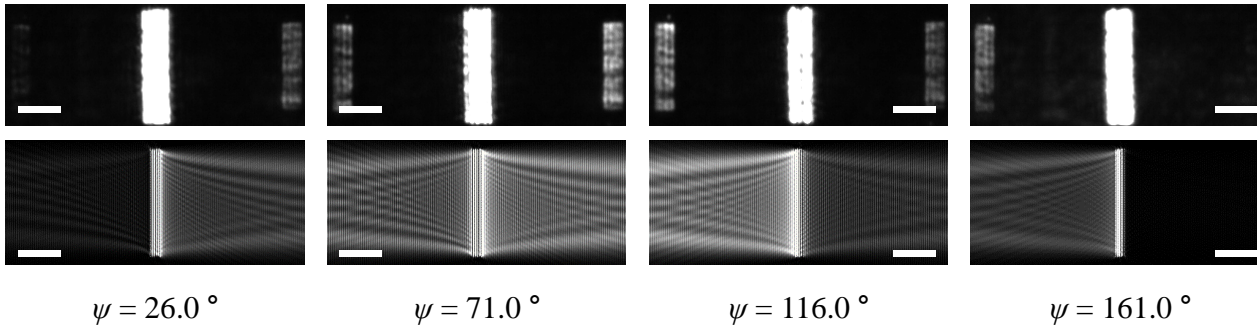
Figure 4.11 Captured images and calculate electric field intensity profiles at ellipticity angles of (a) $\chi = 11.3\,°$ and (b) $\chi = -11.3\,°$ for the cases of $d = 1440$ nm. Scale bars are 10 μm.

(a) $\chi = 11.3$ °

$\psi = 26.0$ ° $\psi = 71.0$ ° $\psi = 116.0$ ° $\psi = 161.0$ °

(b) $\chi = -11.3$ °

$\psi = 26.0$ ° $\psi = 71.0$ ° $\psi = 116.0$ ° $\psi = 161.0$ °
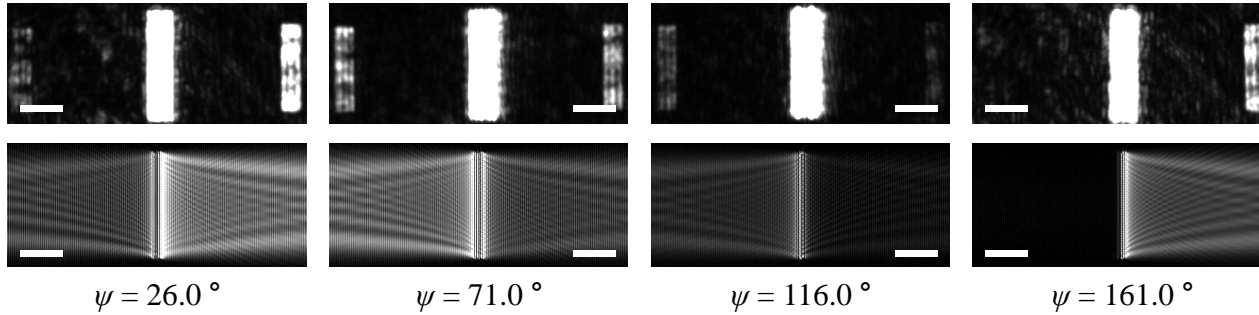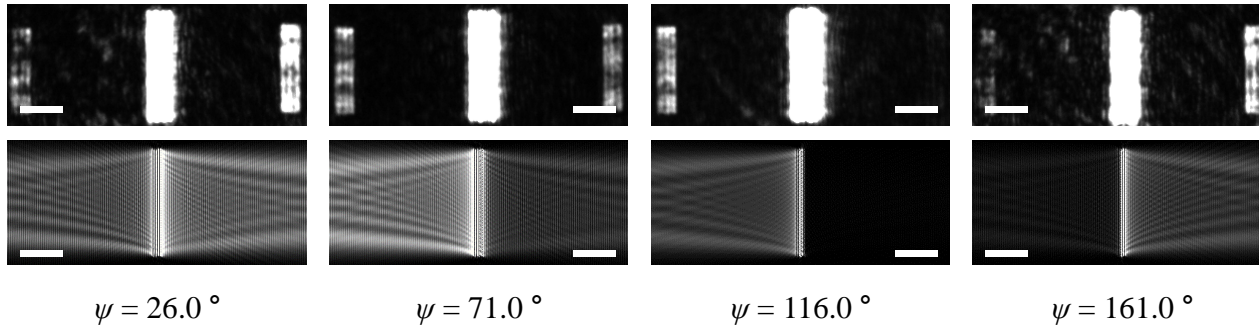
Figure 4.12 Captured images and calculate electric field intensity profiles at ellipticity angles of (a) $\chi = 11.3$ ° and (b) $\chi = -11.3$ ° for the cases of $d = 1200$ nm. Scale bars are 10 μm.
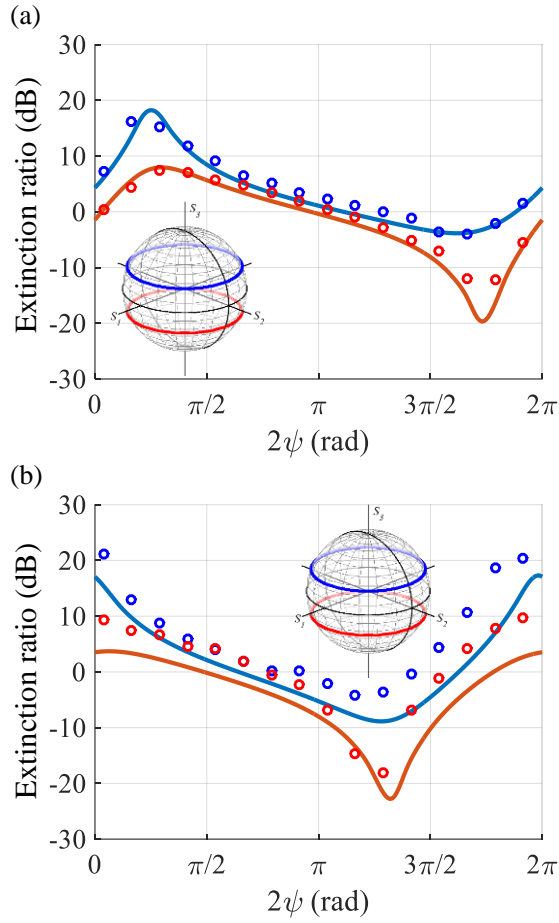
Figure 4.13 Measured extinction ratios for the cases of (a) d = 1440 nm and (b) d = 1200 nm. Insets illustrate SOPs on unit Poincaré spheres.

The extinction ratio is measured by rotating ψ in 16 steps at χ = 11.3 ° and χ = −11.3 °. Intensities I_{x+} and I_{x-} are obtained from brightness at each outcoupler areas of the achieved images, after removing dc level signals. Then the extinction ratios are calculated according to Equation (4.17). Figure 4.13 plots the result. Solid lines are the simulation results that have also been

presented in Figures 4.4(c) and 4.5(c), and dots are the measured extinction ratios. Blue lines and dots denote results of $\chi = 11.3\,°$ and red lines and dots represent those of $\chi = -11.3\,°$ Insets in Figure 3.12 graphically show the given SOPs on a unit radius Poincaré sphere. In the both cases with different d, measured extinction ratios are well matched with the simulation results. High directivity is achieved at the target polarization states. Maxima and minima extinction ratios are obtained as 16.1 dB, -12.2 dB for the case of $d = 1440$ nm, and 21.1 dB, -18.1 dB for the case of $d = 1200$ nm.

4.4 Summary and discussions

In this chapter, generation of SPPs based on an array of hybrid aperture pairs with subwavelength period is investigated. It is shown that directional launching and switching of SPPs can be executed at an arbitrary set of two elliptical polarization states, which are not orthogonal to each other. After verifying the analytic model using the FEM simulations, optical response of the fabricated hybrid aperture pair array is examined. The hybrid aperture pair array with lengths and widths (260 nm, 70 nm,) and (340 nm, 75 nm) is perforated on a 200 nm thick gold film by the FIB milling. Experimental results show high coincidence with the analytic model and numerical results in two different cases. Extinction ratios are achieved as 16.1 dB, −12.2 dB, 21.1 dB, and −18.1 dB at the polarization angles (ψ, χ) of (26.0 °, 11.3 °), (161.0 °, −11.3 °), (4.5 °, 11.3 °), and (116 °, −11.3 °), respectively.

Chapter 5 Compact plasmonic polarimeter

5.1 Introduction

In this chapter, a compact plasmonic polarimeter is proposed based on an X-shaped aperture array. The X-shaped aperture array is composed of a pair of X-shaped aperture of different arm sizes with face-to-face arrangement. Surface plasmon polaritons excited by this aperture array are turned off at a certain elliptically polarized light, so that the X-shaped aperture array acts as an elliptical polarizer of SPPs. Polarization state of normally incident light is detected by reading intensities of SPPs generated by two perpendicular X-shaped aperture arrays. After describing an analytic model of the X-shaped aperture array based on the Jones calculus, design rules of the polarimeter will be presented. Finally, experimental results will be shown with illumination wavelengths of 800 nm, 840 nm, 920 nm, and 980 nm.

5.2 Design of an X-shaped aperture array

5.2.1 Analysis on scattering property of the X-shaped aperture array using the Jones calculus
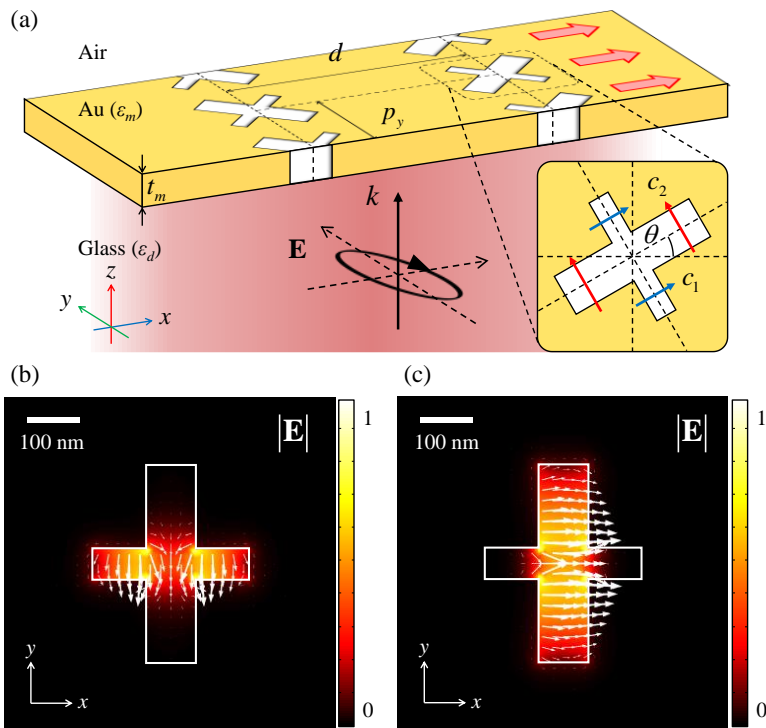
Figure 5.1 (a) Schematic illustration of an X-shaped aperture array. (b, c) Field profiles of two lowest order modes of a single X-shaped aperture.

In Chapter 4, the hybrid aperture array has been discussed that generates SPPs to a single direction for elliptically polarized light. An X-shaped aperture array as shown in Figure 5.1 can be another example of the hybrid

aperture array where the distance between Pair 1 and Pair 2 is zero. In order to guarantee that the X-shaped aperture is equivalent to an overlap of Pair 1 and 2, each arm of the X-shaped aperture should hold independent dipole modes. Figures 5.1(b) and (c) show field profiles of two lowest order modes of the X-shaped aperture. Results of the modes are obtained using a mode analysis based on the FEM. Color maps depict electric field magnitude and arrows represent in-plane instantaneous electric fields. Widths and lengths of the arms along the x-axis and the y-axis are 60 nm, 300 nm, 95 nm, and 380 nm, respectively. Other physical parameters are set as: $\lambda_0 = 840$ nm, $\varepsilon_m = -25.85 + j0.79$ [90]. Calculated field profiles show dipole modes along the each arm. Other higher order modes also exist. However, these higher order modes are rarely excited at the normal incidence, due to zero-averaged field overlap with the equi-phased incident field. It is worthy of noting that magnitude of the electric fields weakens at the center of the aperture due to wide gap distance between metal walls. This causes an effective length of each arm to be reduced.

If the X-shaped aperture only permits two orthogonal dipoles, array of the X-shaped apertures transmits the incident light when an orientation angle of its electric field, or polarization, is matched with the angle of the arm of the X-shaped aperture. That is, the X-shaped aperture array can be considered as a rotated polarizer. The Jones matrix of the rotated polarizer is [85]:

$$\mathbf{M}(\theta) = \mathbf{R}(-\theta)\begin{pmatrix} c_1 & 0 \\ 0 & c_2 \end{pmatrix}\mathbf{R}(\theta), \qquad (5.1)$$

where c_1 and c_2 represent complex scattering coefficients for the incident field which are linearly polarized along the two arms. Equation (5.1) is a general relation that describes any transmitted light through the rotated polarizer. Likewise, Equation (5.1) can characterize SPPs generated by the X-shaped aperture array from the fact that electric field oscillations at the aperture excite SPPs traveling to longitudinal directions. That is, SPPs excited by an X-shaped aperture array, which is periodically arranged along the y-axis, can be explained using an x-pol component of the transmitted Jones vector. Therefore, coupling coefficient of SPPs at given Jones vector $\mathbf{J}$ can be obtained by:

$$c_{\mathrm{SPP}} = \left(\mathbf{M}\mathbf{J}\right)_{11}. \tag{5.2}$$

The proposed X-shaped aperture array consists of two columns of X-shaped apertures that are positioned face-to-face with a distance of d and tilt angle of 45 °. The Jones matrix that gives coupling coefficient of SPPs propagating to the $-x$-direction is written by:

$$\mathbf{M}_{x-} = \mathbf{M}\left(\frac{\pi}{4}\right)e^{-j\frac{\Delta}{2}} + \mathbf{M}\left(\frac{3\pi}{4}\right)e^{j\frac{\Delta}{2}}$$

$$= \begin{pmatrix} \left(c_1 + c_2\right)\cos\dfrac{\Delta}{2} & -j\left(c_1 - c_2\right)\sin\dfrac{\Delta}{2} \\ -j\left(c_1 - c_2\right)\sin\dfrac{\Delta}{2} & \left(c_1 + c_2\right)\cos\dfrac{\Delta}{2} \end{pmatrix}, \tag{5.3}$$

where $\Delta = 2\pi d / \lambda_{SPP}$ is a retarded phase due to traveling of SPPs between the aperture columns. It is possible to extinguish SPPs to the $-x$-direction if there is $\mathbf{J}$ that makes $(\mathbf{M}_{x\text{-}}\mathbf{J})_{11} = 0$. Such $\mathbf{J}_{x\text{-}}$ is calculated from Equation (5.3) as:

$$\mathbf{J}_{x-} = \begin{pmatrix} \left(c_1 - c_2 \right) \sin \dfrac{\Delta}{2} \\ -j\left(c_1 + c_2 \right) \cos \dfrac{\Delta}{2} \end{pmatrix}. \tag{5.4}$$

Decomposition of $\mathbf{J}_{x\text{-}}$ into $\mathbf{J}_R = 1/\sqrt{2}\,(1, -j)^T$ and $\mathbf{J}_L = 1/\sqrt{2}\,(1, j)^T$ gives two coefficient $c_{R\text{-}}$ and $c_{L\text{-}}$:

$$c_{R-} = \frac{1}{\sqrt{2}}\left(c_1 + c_2 \right) \cos \frac{\Delta}{2} + \frac{1}{\sqrt{2}}\left(c_1 - c_2 \right) \sin \frac{\Delta}{2}, \tag{5.5}$$

$$c_{L-} = -\frac{1}{\sqrt{2}}\left(c_1 + c_2 \right) \cos \frac{\Delta}{2} + \frac{1}{\sqrt{2}}\left(c_1 - c_2 \right) \sin \frac{\Delta}{2}, \tag{5.6}$$

where $\mathbf{J}_{x\text{-}} = c_R\mathbf{J}_R + c_L\mathbf{J}_L$. Similarly, $\mathbf{J}_{x+}$, c_{R+} and c_{L+} are obtained by switching the sign of the retarded phase. Denote corollary relations:

$$c_{R+} = -c_{L-}, \tag{5.7}$$

$$c_{L+} = -c_{R-}. \tag{5.8}$$

In order to check the validity of derived relations, the hybrid aperture pair array is revisited. In the case of the hybrid aperture pair, d of Pair 1 and 2 is set as $3\lambda_{SPP} / 4$, which means $\Delta / 2 = 3\pi / 4$. Then $\mathbf{J}_{x-}$ is obtained by:

$$\mathbf{J}_{x-} = -c_2\mathbf{J}_R + c_1\mathbf{J}_L . \tag{5.9}$$

This result corresponds to representation $\mathbf{s}_0$ in the Jones vector form when the distance between Pair 1 and 2 is zero. Likewise, $\mathbf{J}_{x+}$ case gives the SOP of $\mathbf{s}_0^c$, the coincide result.

In summary, the X-shaped aperture array can block SPPs to a certain direction normal to the array period. In other works, the X-shaped aperture array operates as an elliptical polarizer. Allowed SOP, or blocked SOP can be figured out by investigating c_R and c_L. Derived coefficients c_R and c_L will differ according to the wavelength, but it is still possible to find appropriate values of c_R and c_L. Therefore, the X-shaped aperture array can function as a broadband elliptical polarizer of SPPs.

Before further examinations, properties of the X-shape aperture array at a certain target wavelength are investigated in order to determine geometric parameters of the X-shaped aperture. The standard wavelength is chosen to be 840 nm, considering operation wavelengths of experiment apparatus. Detailed description about experimental setup and conditions will be presented in Section 5.4. Similar to the design strategy proposed in Section 4.2.2, scattering properties of a single aperture pair array are analyzed firstly considering the X-shaped aperture as a sum of the two arrays.

(a)

c (dB)

(270, 360)
$c = 1.252$

(b)

δ (rad)

(270, 360)
$\delta = 45.05°$
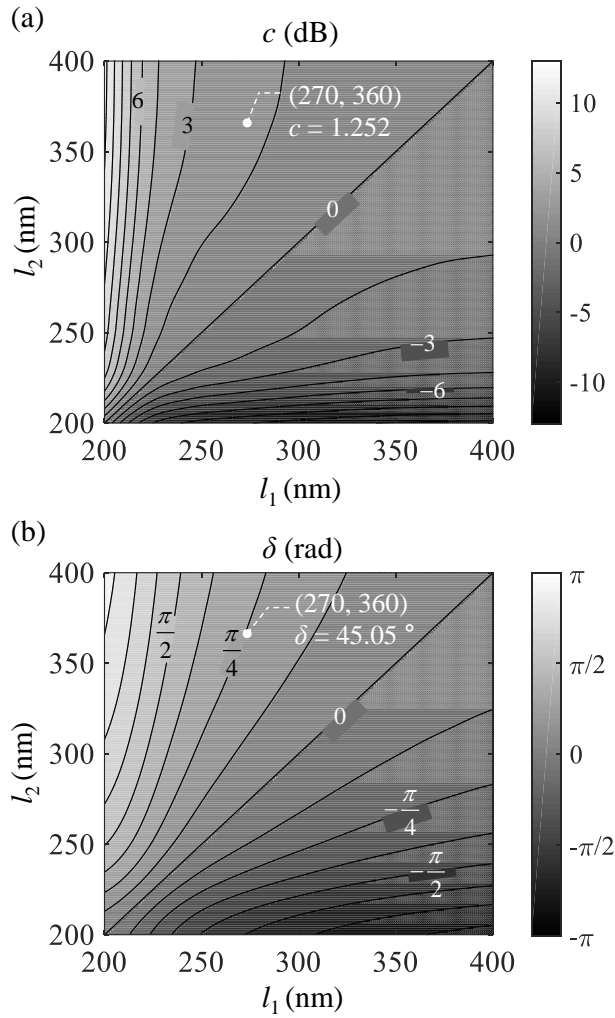
Figure 5.2 Contour maps of (a) the coupling coefficient c and (b) the phase difference δ according to length of the rectangular apertures.

Figure 5.2 shows results of the coupling ratio c and the phase difference δ of SPPs following Equations (4.4) and (4.5) with respect to lengths of aperture pair array. Geometric and physical parameters are assigned as: wavelength of the incident light $\lambda_0 = 840$ nm, dielectric constants of gold and

dielectric substrate, $\varepsilon_m = -25.85 + j0.79$, $\varepsilon_d = 2.11$, wavelength of the SPP $\lambda_{SPP} = 824$ nm, distance between the array columns $d = 620$ nm, period along the y-axis $p_y = 360$ nm, and thickness of the metal film $t_m = 300$ nm. Aspect ratio of the aperture is fixed as 4 so that the width is a quarter of given length. Thickness of the gold film and range of the aperture lengths are set to avoid resonance at the aperture since the resonance can induce abrupt change in c and δ.
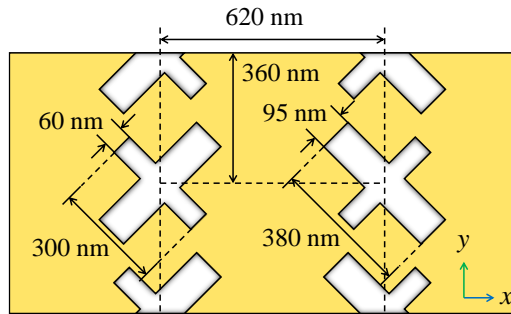
Figure 5.3 A top-view of determined X-shaped aperture array.

Here, 270 nm and 360 nm of l_1 and l_2 are chosen respectively that give parameters of $c = 1.252$ and $\delta = 45.05$ °. When two aperture pairs are overlapped and form the X-shaped aperture, however, effective lengths of the arms shrink due to expansion of gap size at the overlap region. Thus, the arm lengths should be longer than the aperture lengths to make the X-shaped aperture array show the same c and δ. Additional parametric study of the arm lengths is executed and finds out additional lengths of 30 nm and 20 nm for each arm, which correspond to about a one-third of the widths. Geometric parameters of the final X-shaped aperture array is as shown in Figure 5.3,

lengths and widths are (300 nm, 60 nm) for the arm 1, and (380 nm, 95 nm) for the arm 2. Coupling parameters of the determined X-shape aperture array are, $c = 1.438$ and $\delta = 44.65$ °.
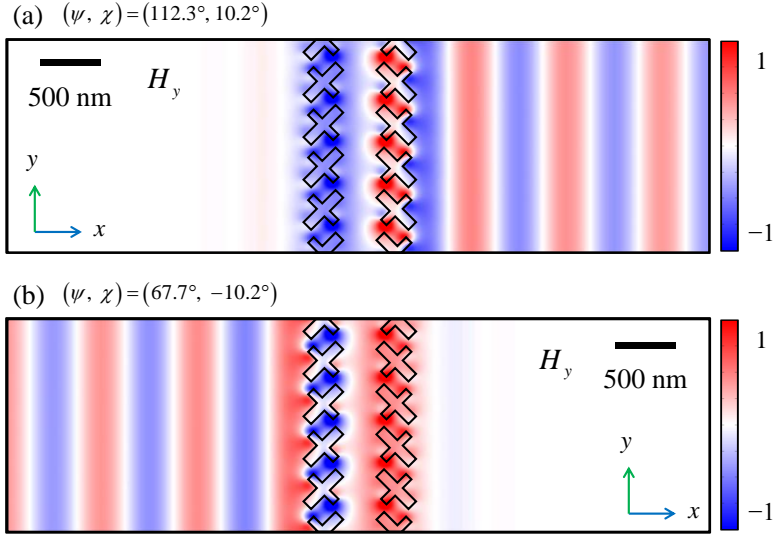
(a) $(\psi, \chi) = (112.3°, 10.2°)$

(b) $(\psi, \chi) = (67.7°, -10.2°)$

Figure 5.4 Normalized H_y-field profiles at the xy-plane 20 nm above the surface illuminated by the give SOPs.

According to Equations (4.12), (4.13), and (4.14), polarization angles ψ and χ at directional launching condition of SPPs are (112.3 °, 10.2 °) and (67.7 °, −10.2 °). The first pair of angles make SPPs propagate to the +x-direction, and the second pair to the −x-direction. Figure 5.4 shows field profiles of SPPs, Hy-field, when the input beam is polarized as the given polarization angles. Color maps represent H_y-fields in the xy-plane at 20 nm above the metal surface. It is clearly seen that SPPs are generated to a single direction as expected with high directivity. Extinction ratios are 25.5 dB for

the case of Figure 5.4(a) and -25.5 dB for the case of Figure 5.4(b), following Equation (4.17). Compared with the hybrid aperture pair array, the X-shape aperture pair operates symmetrically with respect to the helicity of the incident light. The reason is that the X-shaped aperture array have even geometry along the x-axis, while the hybrid aperture pair array does not.

5.2.2 Broadband polarizer-like property of the X-shaped aperture array

The X-shaped aperture array blocks the incident light of selected SOP when SPPs to a single direction is considered as a transmitted wave. The forbidden SOP is determined following Equations (5.5) and (5.6). I introduce parameters that characterize the polarizer-like property of the X-shaped aperture array similar to Equations (4.4) and (4.5) as:

$$c = \left| \frac{c_{R+}}{c_{L+}} \right|, \tag{5.10}$$

$$\delta = \angle c_{R+} - \angle c_{L+}. \tag{5.11}$$

The coupling ratio c and the phase difference δ are functions of a wavelength since c_1, c_2, and Δ vary according to the wavelength. c and δ can be obtained by imposing the circularly polarized light to the X-shaped aperture array, rather than achieving all the subcomponents c_1, c_2, and Δ. Let the RCP light illuminate the X-shaped aperture array. Based on the Jones

matter as Equation (5.3), SPPs to each direction is given by:

$$\left(\mathbf{M}_{x+}\mathbf{J}_{\mathrm{R}}\right)_{11} = \frac{1}{\sqrt{2}}\left(c_1 + c_2\right)\cos\frac{\Delta}{2} + \frac{1}{\sqrt{2}}\left(c_1 - c_2\right)\sin\frac{\Delta}{2}, \quad (5.12)$$

$$\left(\mathbf{M}_{x-}\mathbf{J}_{\mathrm{R}}\right)_{11} = \frac{1}{\sqrt{2}}\left(c_1 + c_2\right)\cos\frac{\Delta}{2} - \frac{1}{\sqrt{2}}\left(c_1 - c_2\right)\sin\frac{\Delta}{2}. \quad (5.13)$$

Noticing that $(\mathbf{M}_{x+}\mathbf{J}_{\mathrm{R}})_{11} = c_{\mathrm{R+}}$ and $(\mathbf{M}_{x-}\mathbf{J}_{\mathrm{R}})_{11} = -c_{\mathrm{L+}}$, the coupling parameters c and δ can be rewritten as:

$$c = \left|\frac{\left(\mathbf{M}_{x+}\mathbf{J}_{\mathrm{R}}\right)_{11}}{\left(\mathbf{M}_{x-}\mathbf{J}_{\mathrm{R}}\right)_{11}}\right|, \quad (5.14)$$

$$\delta = \angle\left(\mathbf{M}_{x+}\mathbf{J}_{\mathrm{R}}\right)_{11} - \angle\left(-\mathbf{M}_{x-}\mathbf{J}_{\mathrm{R}}\right)_{11}. \quad (5.15)$$

The polarization angles $\psi_\pm$ and $\chi_\pm$ of the forbidden SOP, which turn off SPPs to propagate to the $\pm x$-direction, are then obtained by:

$$\psi_\pm = \frac{\pi \pm \delta}{2}, \quad (5.16)$$

$$\chi_\pm = \pm\arctan\left(\frac{c-1}{c+1}\right), \quad (5.17)$$

71

where sign of Equations (5.16) and (5.17) corresponds to the case of $-x$-direction for the plus and $+x$-direction for the minus, respectively in the same order.
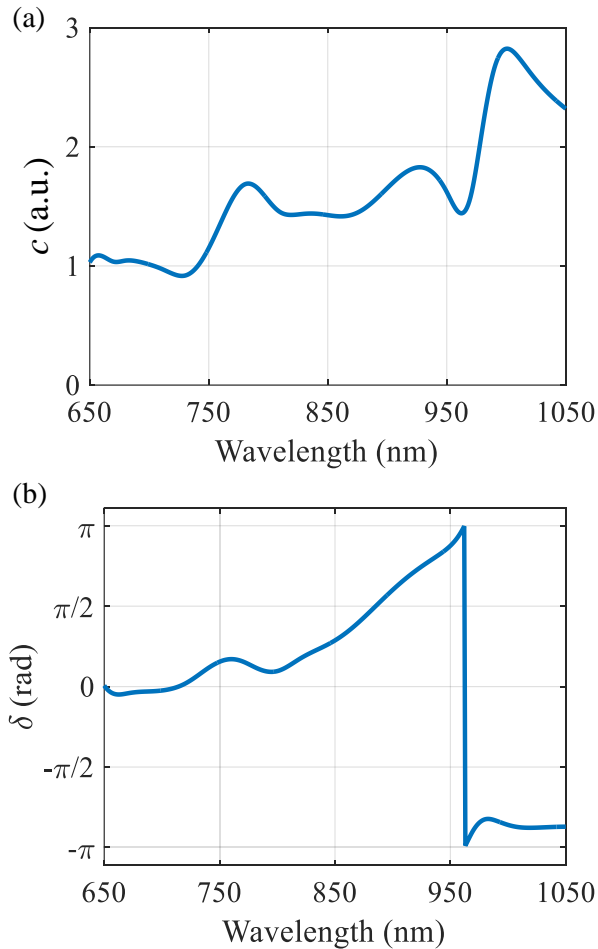
Figure 5.5 Coupling parameters (a) c and (b) δ with respect to the wavelength of the incident light.

Figure 5.5 shows the coupling parameters c and δ with respect to the wavelength of the incident light. Amplitude and phase of near-fields carried

by SPPs are measured when the X-shaped aperture array is illuminated by normally incident RCP light. Then c and δ are computed based on Equations (5.14) and (5.15). Geometric and physical parameters are set as the same as the FEM simulations that achieve results of Figure 5.4. Considering material dispersion, dielectric constants of a gold film and a glass substrate are given according to the textbook [90]. Wavelength window ranges from 650 nm to 1050 nm, which is about ± 200 nm from the reference wavelength of 840 nm.

Each point of Figure 5.5 informs the forbidden SOPs at each wavelength. For example, at 850 nm, $c = 1.426$ and $\delta = 51.68$ °. Corresponding polarization angle sets of the forbidden SOPs are (115.8 °, 10.0 °) at the –x-direction and (64.2 °, –10.0 °) at the +x-direction. Likewise, forbidden SOPs will be (103.9 °, 4.0 °), (76.1 °, –4.0 °) at the wavelength of 750 nm, and (15.8 ° 20.1 °), (164.2 °, –20.1 °) at the wavelength of 980 nm. Extinction ratios following the definition of Equation (4.17) are calculated at previously mentioned wavelengths to verify that the parameters c and δ can describe the function of the X-shaped aperture array as the polarizer.

Results plotted in Figure 4.6. show that peaks of extinction ratios appear at the expected forbidden SOPs. High extinction ratio along a direction indicates that SPPs to the other direction are turned off. Therefore, properties of the SPP polarizer can be properly characterized by the coupling parameters c and δ, which are figured out from Equations (5.14) and (5.15).
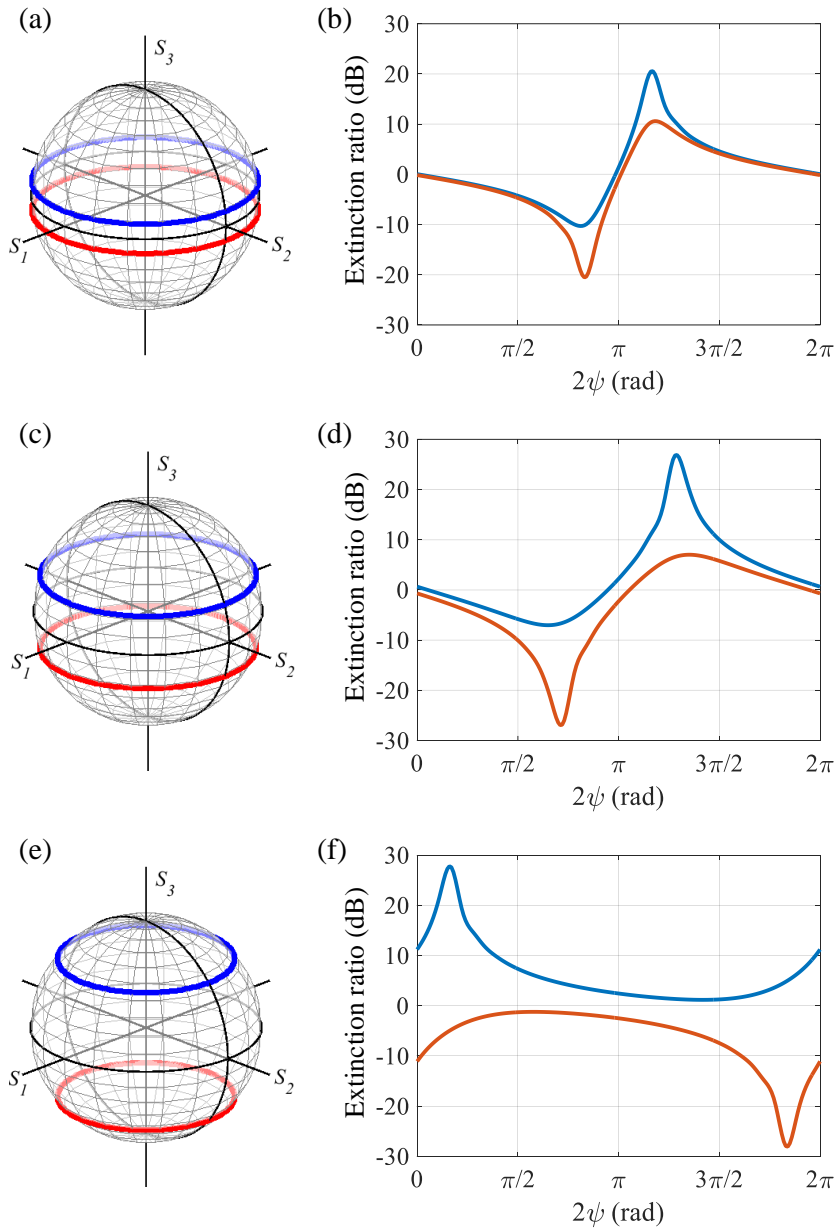
Figure 5.6 Poincaré sphere representation of given polarization states and corresponding extinction ratios at the wavelength of (a, b) 750 nm, (c, d) 850 nm, and (e, f) 980 nm, respectively.

Meanwhile, it is worthy of noting that c reaches about 1, and δ about 0 at the wavelengths below 750 nm, which result in difference between the polarization angles $\psi_+ - \psi_-$ and $\chi_+ - \chi_-$ to be zero. This implies that the X-shaped aperture array cannot split SPPs according to the SOP of the incident light, or the forbidden SOPs are degenerated. Hence, the X-shaped aperture array does not play the role of a polarizer in this wavelength range.

5.3 Single-shot characterization of a polarization state using the X-shaped aperture array

5.3.1 Configuration of the polarimeter based on the X-shaped aperture array
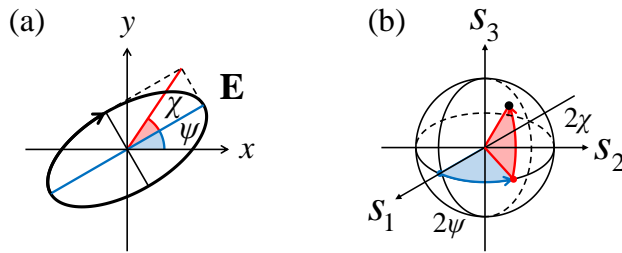
Figure 5.7 (a) Polarization ellipse and (b) corresponding SOP representation using a unit Poincaré sphere.

A polarizer is used for apparatus that measures an SOP of light. Full characterization of an arbitrary SOP can be achieved by detecting transmitted power through a set of different polarizers. TWhe SOP vector, which is a unit vector on the Poincaré sphere, is defined by:

$$s_1 = \cos(2\chi)\cos(2\psi), \qquad (5.18)$$

$$s_2 = \cos(2\chi)\sin(2\psi), \qquad (5.19)$$

$$s_3 = \sin(2\chi). \qquad (5.20)$$

From the above definition, $\mathbf{s} = (1, 0, 0)$ represents a linear polarization along the x-axis, $(-1, 0, 0)$ the y-axis, $(0, 1, 0)$ an axis with an angle of 45 °, $(0, -1, 0)$ with an angle of 135 °, $(0, 0, 1)$ the RCP, and $(0, 0, -1)$ the LCP. Assuming six measuring polarizers that transmit SOPs representing each end of the basis, the SOP components of the measured light are given by:

$$s_1 = \frac{I_x - I_y}{I_x + I_y}, \tag{5.21}$$

$$s_2 = \frac{I_{x+y} - I_{x-y}}{I_x + I_y}, \tag{5.22}$$

$$s_3 = \frac{I_R - I_L}{I_x + I_y}, \tag{5.23}$$

where I_x, I_y, I_{x+y}, I_{x-y}, I_R, and I_L denote intensities of the measured light through each polarizer. This shows that the SOP vector can be fully characterized by probing transmitted power through the six polarizers. Probes can be reduced to the number of four, whose SOPs are represented by a tetrahedron when inscribed in the Poincare sphere [102].
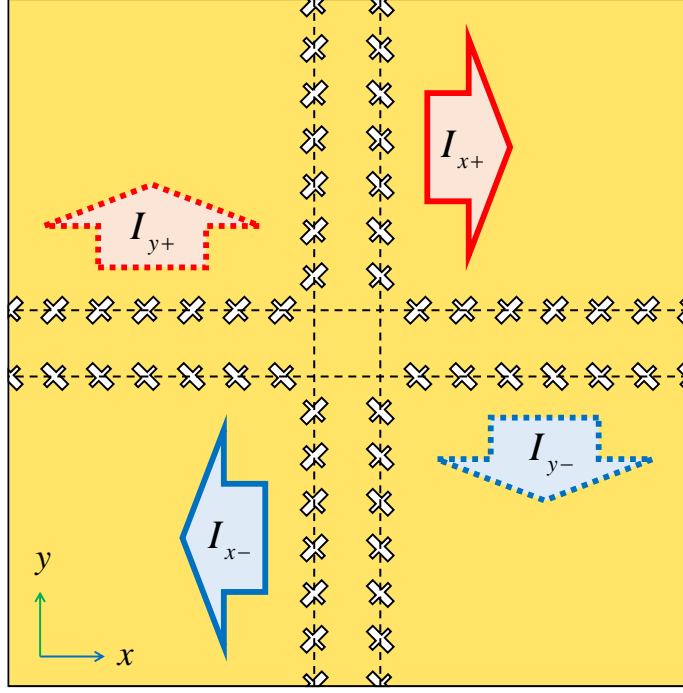
Figure 5.8 Configuration of a polarimeter based on perpendicular arrangement of the X-shape aperture array.

In the previous section, it is shown that the X-shaped aperture array functions as an elliptical polarizer of SPPs. Coupling coefficient of SPPs propagating to the $+x$-direction that is excited by the SOP with the Jones vector of $\mathbf{J} = a_R\mathbf{J}_R + a_L\mathbf{J}_L$ can be expressed as $(\mathbf{M}_{x+}\mathbf{J})_{11}$, according to the explanations of the previous section. Intensity of SPP fields traveling to the $+x$-direction is then written as:

$$I_{x+} = I_0 \left[c^2 a_R^2 + a_L^2 + 2c a_R a_L \cos\left(2\psi + \delta\right) \right], \qquad (5.24)$$

where c and δ are the coupling parameters following Equations (5.10) and (5.11), respectively. Similarly, intensity to the $-x$-direction is

$$I_{x-} = I_0 \left[a_R^2 + c^2 a_L^2 + 2ca_R a_L \cos\left(2\psi - \delta\right) \right]. \qquad (5.25)$$

Counter-clockwise rotation of the entire X-shaped aperture array as shown in Figure 5.8 will excite additional SPPs to the y-directions:

$$I_{y+} = I_0 \left[c^2 a_R^2 + a_L^2 - 2ca_R a_L \cos\left(2\psi + \delta\right) \right], \qquad (5.26)$$

$$I_{y-} = I_0 \left[a_R^2 + c^2 a_L^2 - 2ca_R a_L \cos\left(2\psi - \delta\right) \right]. \qquad (5.27)$$

The SOP vector of the incident light can be analyzed using the intensities I_{x+}, I_{x-}, I_{y+}, and I_{y-} as:

$$s_1 = \left(\frac{c^2 + 1}{2c \cos \delta} \right) \frac{I_{x+} + I_{x-} - I_{y+} - I_{y-}}{I_{x+} + I_{x-} + I_{y+} + I_{y-}}, \qquad (5.28)$$

$$s_2 = \left(\frac{c^2 + 1}{2c \sin \delta} \right) \frac{-I_{x+} + I_{x-} + I_{y+} - I_{y-}}{I_{x+} + I_{x-} + I_{y+} + I_{y-}}, \qquad (5.29)$$

$$s_3 = \left(\frac{c^2 + 1}{c^2 - 1} \right) \frac{I_{x+} - I_{x-} + I_{y+} - I_{y-}}{I_{x+} + I_{x-} + I_{y+} + I_{y-}}. \qquad (5.30)$$

That is, it is possible to characterize any SOP of the incident light with a single-shot measurement by detecting optical powers delivered by SPPs to four directions. Furthermore, the parameters c and δ, which are obtained from coupling coefficients of the X-shaped aperture pairs, are used as calibration factors. Datasheet of the calibration factors at given wavelength should be acquired first, before starting the measurement.

5.3.2 Specification of operation bandwidth

If denominators in parentheses of Equations (5.28), (5.29) and (5.30) become zeros, the SOP vector cannot be obtained. There are two conditions that the denominators become zeros: 1) $c = 1$, and 2) $\delta = n\pi / 2$, where n is an integer number. Operation bandwidth of the determined polarimeter can be specified by examining distribution of c and δ with respect to the wavelength. In the case of the proposed X-shaped aperture array, wavelengths below 750 nm violate the first criterion, and around 885 nm and 960 nm violate the second criterion, according to Figure 5.5.

On the other hand, the operation bandwidth can be engineered to cover certain target range by inspecting the calibration factor c and δ to regulate the criteria under given geometric and physical parameters. It will be a good approach to make δ be 45 ° at the center wavelength first, for δ to keep away from both 0 ° and 90 °.

5.4 Experimental demonstration

5.4.1 Fabrication and measurement setup
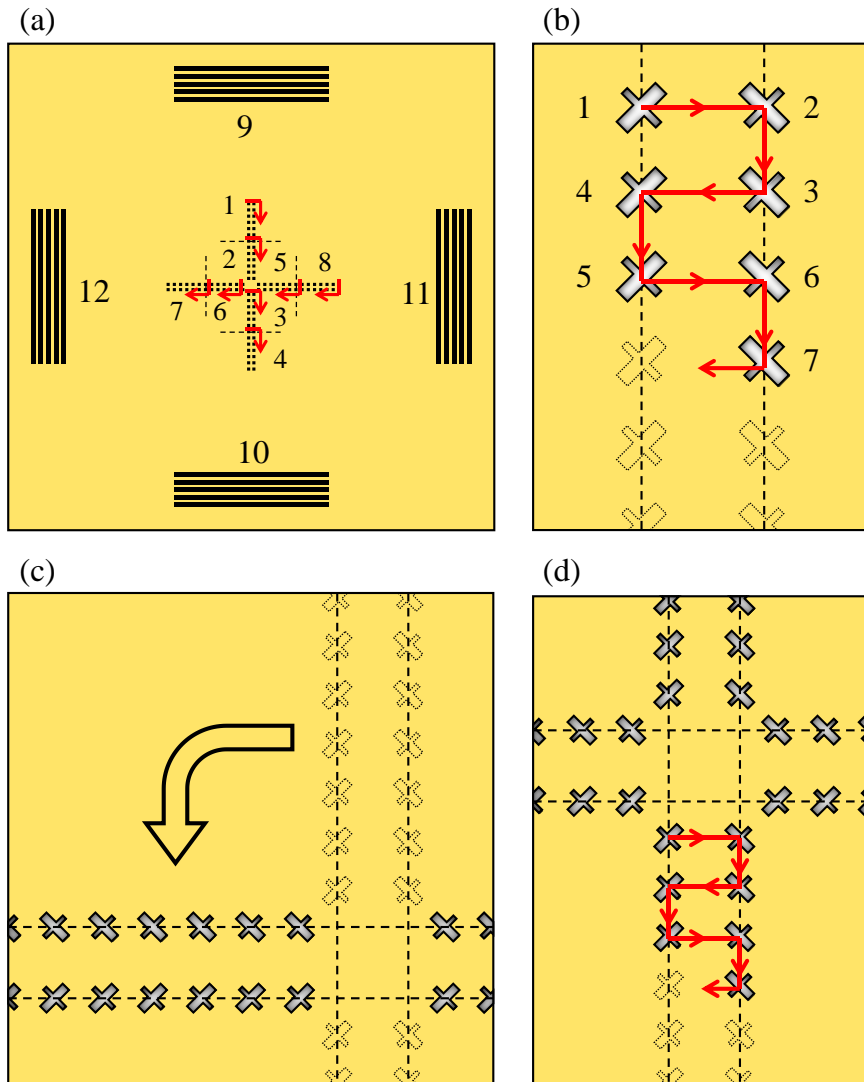
Figure 5.9 Schematic illustration of FIB milling sequence.

FIB (FEI, Quanta 200 3D) milling is used for fabrication of the X-shaped aperture array and the outcouplers. The X-shaped apertures are perforated at a single exposure of 10 pA of current and 30 kV on a 300 nm thick gold film deposited on a 1 mm thick piecewise slide glass (Marienfeld, plain) by e-beam evaporator (KVT, KVE-3004). Polygon function is used to outline the geometry of the X-shaped aperture. Coordinates of polygon vertices are assigned counter-clockwise manner starting at 12 o'clock, regardless of a tilt angle of the X-shape aperture.
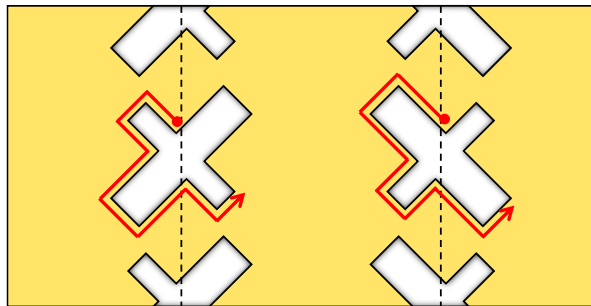
Figure 5.10 Coordinate assignment of the X-shaped aperture based on a polygon function.

Milling sequence of the entire device is allocated as illustrated in Figure 5.9 in order to guarantee the precise geometry. At first, 14 periods of the X-shaped aperture pairs along the *y*-direction are perforated 4 times from the top to the bottom. Each aperture is fabricated row-by-row in a zigzag manner as shown in Figure 5.9 (b). At the center, an additional translation of 1.4 μm is inserted in order to avoid overlap among the horizontally and vertically arranged apertures. The aperture array along the horizontal axis is made

according to the similar procedure after rotating a sample holder 90 by degrees counter-clockwise as depicted in Figures 5.9(c) and (d). Here, in order for fine alignment between the vertical and horizontal array, the aperture arrays near the center are fabricated first, rather than the straight sequence from the top to the bottom.

(a)

(b)

(c)

(d)
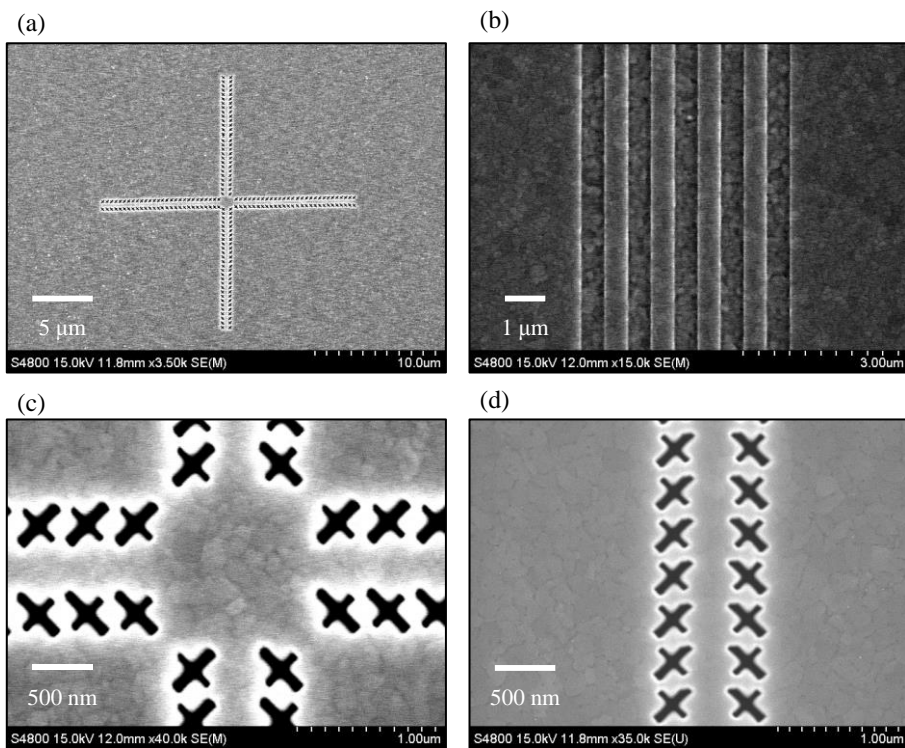
Figure 5.11 SEM images of (a) the proposed polarimeter, (b) the outcoupler, (c) magnified views at the center area of the polarimeter, and (d) the X-shaped aperture array.

After that, the outcouplers are located with the same process. The 90 degrees rotation of the sample holder is executed between the vertical ones

and horizontal ones, fixing the geometry with vertical shape. The outcouplers are placed at the four sides, 25 μm away from the center. Geometry of the outcoupler is the same as what has been used in Chapter 4: 880 nm period with 0.5 fill factor, 5 periods, 80 nm depth, and 18 μm length.
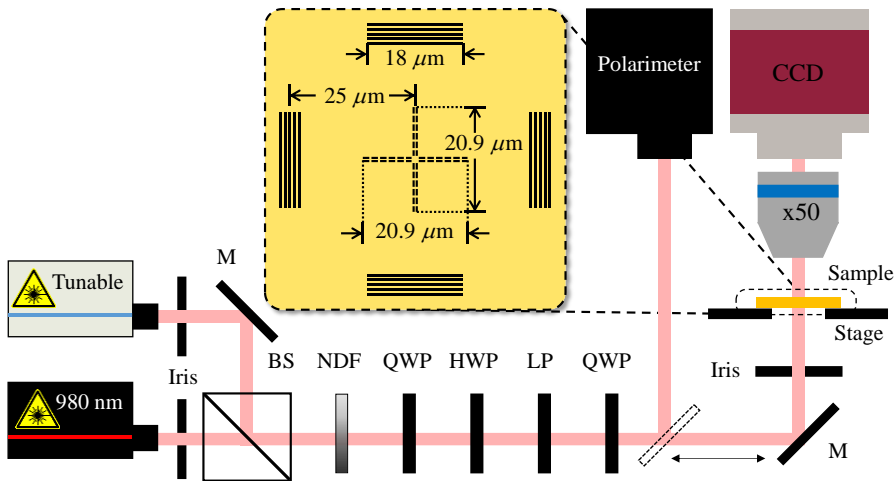
Figure 5.12 Experimental setup. Inset illustrates a top-view of the sample. M: mirror, BS: beam-splitter, NDF: neutral-density filter, QWP: quarter-wave plate, HWP: half-wave plate, LP: linear polarizer, CCD: charge-coupled device, and x50: objective lens of x50.

Experiment setup is made based on a Ti:Sapphire tunable laser and a continuous wave laser of 980 nm wavelength. The tunable laser covers wavelengths from 700 nm to 920 nm (Sirah, Matisse TR). Beam paths of the two lasers are combined using a beam-splitter. Output powers of the laser beams are set about 200 ~ 300 mW, admitting some amount of variation with respect to the wavelength. The other part of the experimental setup is similar to the apparatus used in Chapter 4. A set of a polarizer and wave plates with

anti-reflection coatings are placed after the beam-splitter to produce elliptical polarization states. The center wavelength of the X-shaped aperture is set to be 840 nm at first, which is mentioned in Section 5.2.1, after considering operation bandwidth of the tunable laser and optical elements. Measurement of images of the illuminated sample and corresponding SOPs are executed using the CCD camera (Allied Vision, Mako G-223) and the commercial polarimeter (Thorlabs, PAX5710IR-T), which are the same as the equipment introduced in Chapter 3.

5.4.2 Field profiles and measured polarization states

In order for verification of the broadband operation, the fabricated sample is tested at wavelengths of 760 nm, 800 nm, 840 nm, 920 nm, and 980 nm. Due to the wavelength coverage of the tunable laser, 980 nm wavelength is generated using the separate continuous wave laser as shown in Figure 5.12.

At first, the calibration factors c and δ are measured with respect to the given wavelengths. According to Equations (5.28), (5.29), and (5.30), measured intensities can be related to the SOP vector after achieving datasheets of c and δ over the operation wavelengths. The calibration factors can be obtained experimentally using Equations (5.14) and (5.16). Equation (5.14) tells that the coupling ratio between intensities along the x-directions or the y-directions quantifies c when the incident light is given by the RCP or LCP. Value of c is computed by an average of four different coupling ratios since there are two sets of outcouplers and two given SOPs.

In the case of δ, difference of orientation angles that turn off SPPs to each x-direction or y-direction corresponds to δ. Table 5.1 notes orientation

angles of polarizations at each wavelength when each outcoupler turns off. Column labels of the table, right, left, up, and down, denote positions of the each outcouplers. During the experiment, combinations of the linear polarizer and the half-wave plate are recorded by inspecting the brightness at each outcoupler to be the darkest. Then the SOP is detected using the polarimeter at each recorded condition. Value of δ is calculated as a mean of two angle differences, which are obtained from the horizontal and the vertical sets of outcouplers, respectively.

Table 5.1 Orientation angles of polarizations at extinguishments of each outcoupler.

Wavelength (nm)	Right (°)	Left (°)	Up (°)	Down (°)
760	92.8	91.1	2.9	175.6
800	97.8	85.1	9.0	173.0
840	104.2	70.8	16.0	157.5
920	153.1	30.1	64.2	107.2
980	166.7	19.0	82.7	102.4

Figure 5.13 shows the measured calibration factors (dots) compared with the simulation results (solid lines). It is shown that the phase factor δ is well matched among the measured ones and calculated ones. However, in a case of amplitude factor c, there is some amount of overshoot at longer wavelengths. Both fabrication errors and nonlinear sensitivity curve of the CCD camera can contribute to this result.
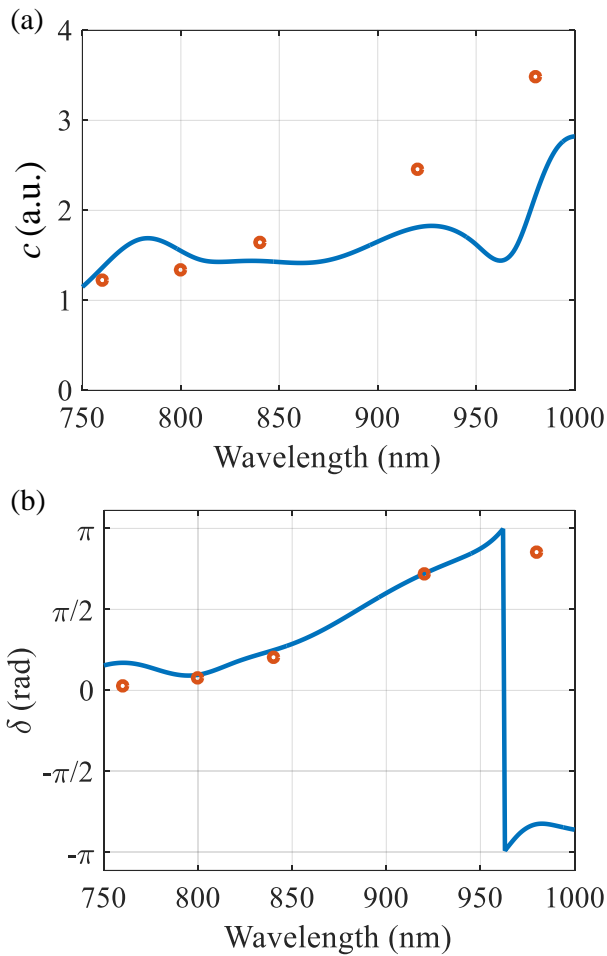
Figure 5.13 Measured calibration factors c and δ (red dots) at wavelengths of 760 nm, 800 nm, 840 nm, 920 nm, and 980 nm.

Revisiting the issue about the operation bandwidth in Section 5.3.2, it is worth to noting that the calibration factor δ of the 760 nm case violates the second criteria that is discussed in section 5.3.2: $\delta = 4.5$ °, which is close to 0. Therefore, characteristics as the polarimeter of the proposed device will be demonstrated at wavelengths of 800 nm, 840 nm, 920nm, and 980 nm from

now on. Results of the 760 nm will be discussed in Section 5.4.3.

Figures 5.14 and 5.15 show CCD images at given SOPs at each wavelength. In order for comparison, electric field intensity profiles in the *xy*-plane at 100 nm above the surface based on the dipole model simulation are depicted under corresponding CCD images. The captured CCD images and calculated field profiles show high coincidence with each other. Brightness level at the center of the outcouplers is lower due to the void at the center where the vertical and horizontal array intersect.

Ten different polarization states, which correspond to the end of each axis s_1, s_2, and s_3, and other four more elliptical polarization states, are measured. Intensities are achieved by averaging the signal inside each outcoupler region and eliminating dc noise from captured images. States of polarization vectors are computed then following Equations (5.28), (5.29), and (5.30). The calibration factors c and δ follow the measured results.

$(\psi, \chi) = (22.5\,^{\circ}, 20\,^{\circ})$

$\lambda_0 = 800$ nm	$\lambda_0 = 840$ nm	$\lambda_0 = 920$ nm	$\lambda_0 = 980$ nm
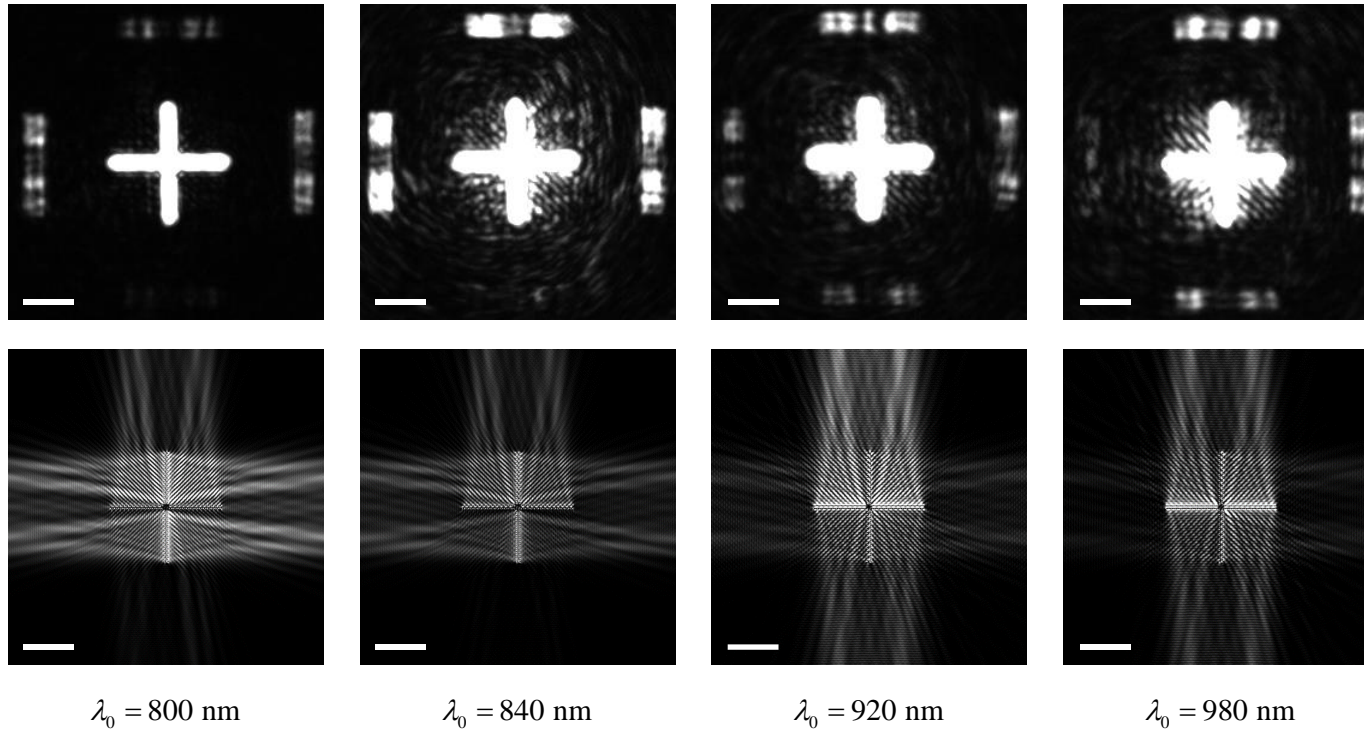
Figure 5.14 Captured CCD images and corresponding calculated electric field intensity profiles for the given SOP $(\psi, \chi) = (22.5\,^{\circ}, 20\,^{\circ})$. Scale bars are 10 μm.

$(\psi, \chi) = (157.5\,°, -20\,°)$

$\lambda_0 = 800$ nm $\lambda_0 = 840$ nm $\lambda_0 = 920$ nm $\lambda_0 = 980$ nm
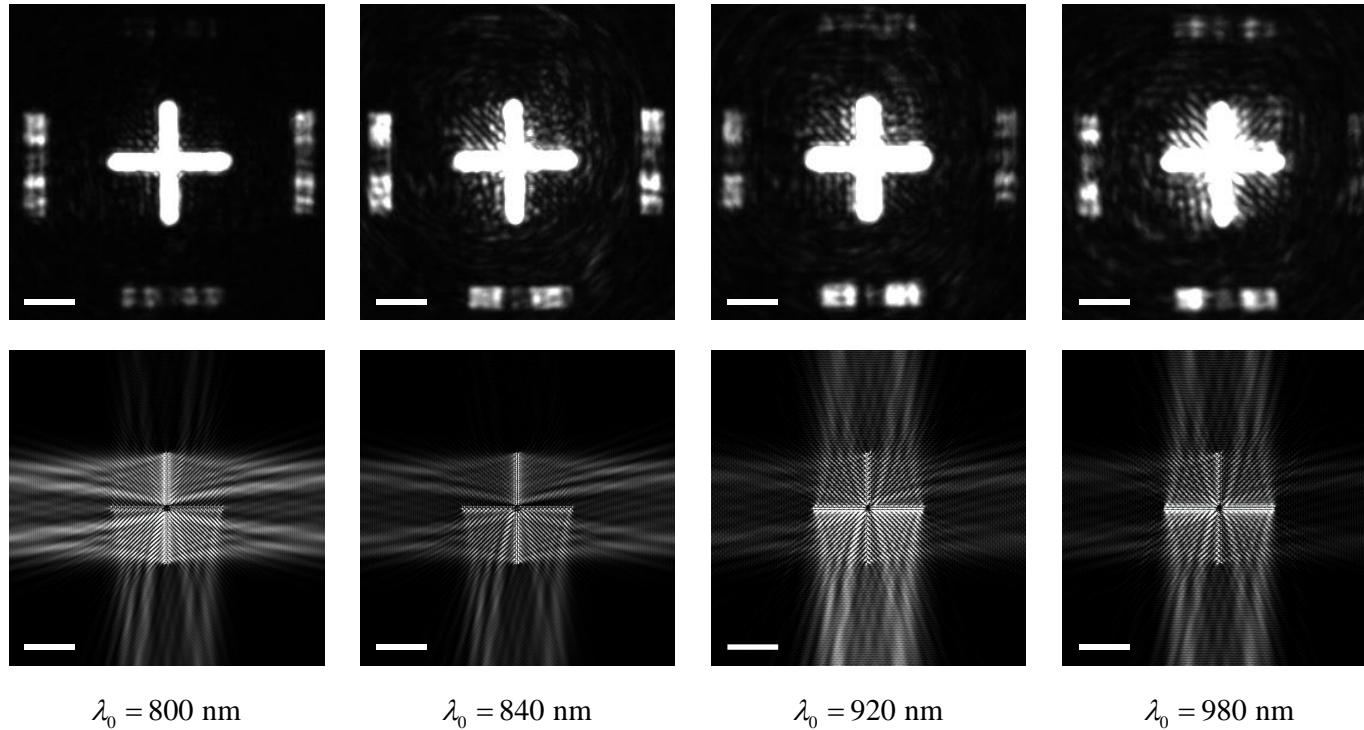
Figure 5.15 Captured CCD images and corresponding calculated electric field intensity profiles for the given SOP $(\psi, \chi) = (157.5\,°, -20\,°)$. Scale bars are 10 μm.

Figure 5.16 shows the obtained SOPs represented on the unit Poincaré sphere. The first six measurements, which correspond to linear polarizations with orientation angles of 0 °, 45 °, 90 °, and 135 °, and two circular polarizations, are illustrated. Blue dots represent the SOP of the incident light, and red dots indicate measured SOPs using the proposed polarimeter. It is shown that each point on the sphere shows high coincidence. Likewise, measurement results of the four additional elliptical polarization states given by $(\psi, \chi) = (22.5°, \pm 20°), (157.5°, \pm 20°)$ are shown in Figure 4.17. The red dots are located adjacent to the blue dots in the same way.

In order to quantify the accuracy of the proposed polarimeter, introduce deviations of the orientation angle and the ellipticity angle as:

$$\Delta \psi = \sqrt{\frac{\sum \left(\psi_m - \psi_{\mathrm{ref}}\right)^2}{n}}, \qquad (5.31)$$

$$\Delta \chi = \sqrt{\frac{\sum \left(\chi_m - \chi_{\mathrm{ref}}\right)^2}{n}}, \qquad (5.32)$$

where subscript m denotes the measurement value, and ref denotes the given value. $n = 10$ here, which is the number of the measurement. Measured polarization angles ψ_m and χ_m are obtained using Equations (5.18), (5.19) and (5.20).
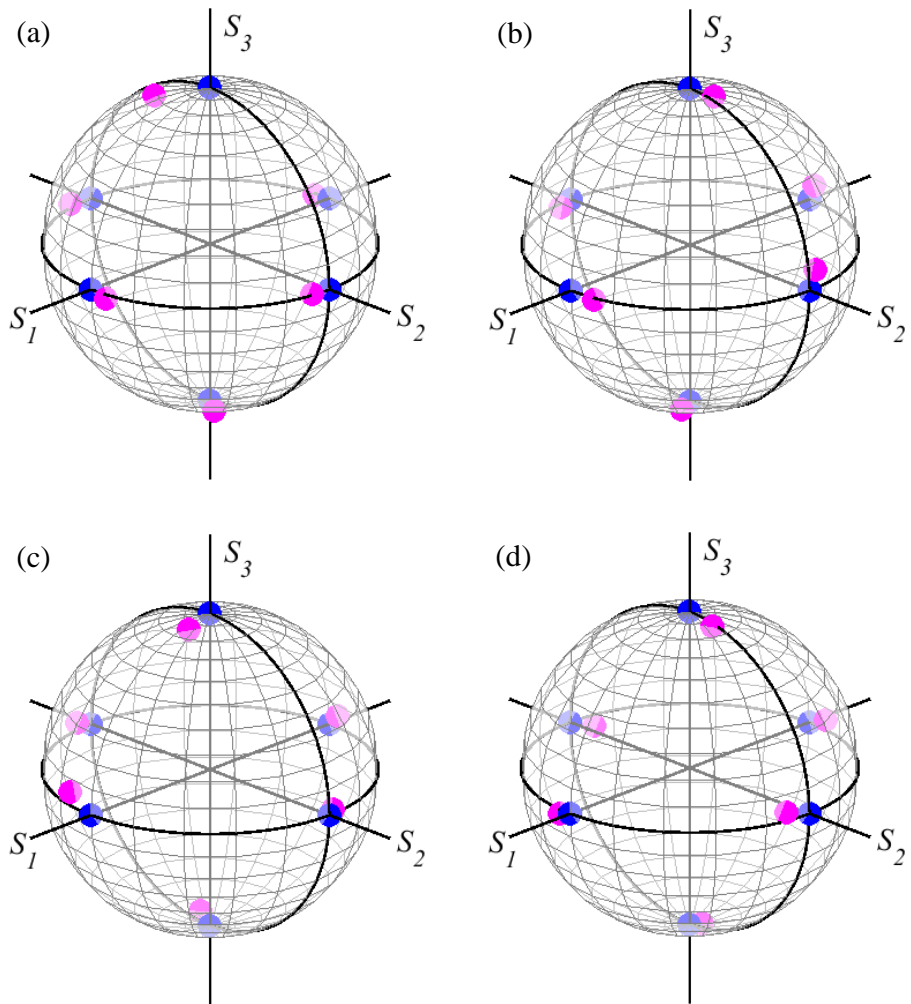
Figure 5.16 Poincaré sphere representation of the measured SOPs for linear and circular polarizations at the wavelength of (a) 800 nm, (b) 840 nm, (c) 920 nm, and (d) 980 nm.
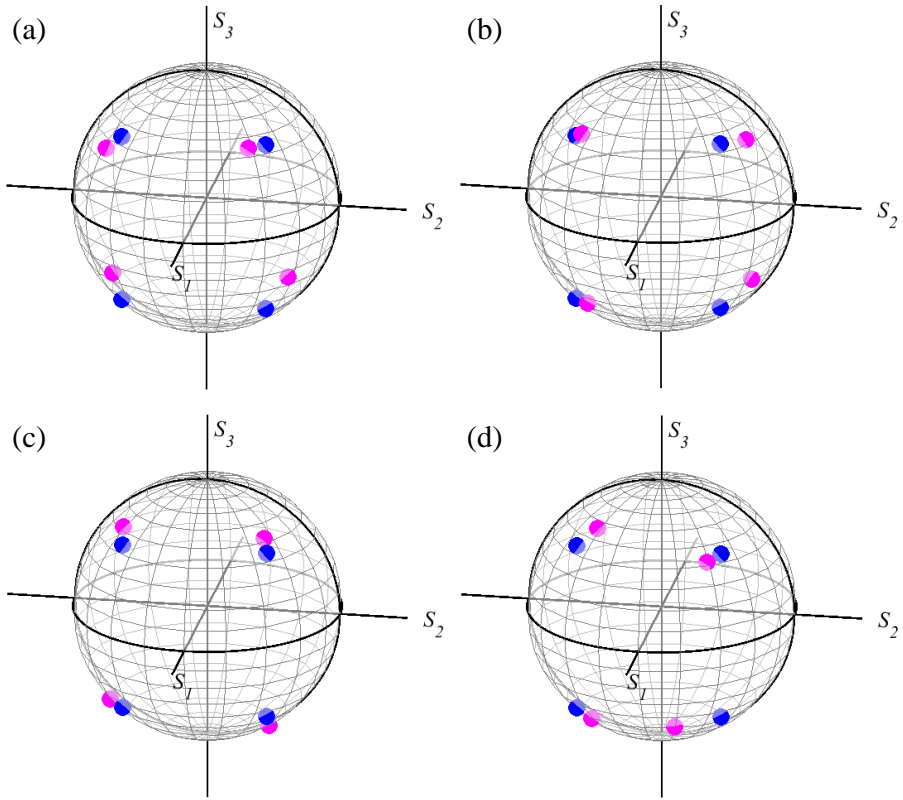
Figure 5.17 Poincaré sphere representation of the measured SOPs for elliptical polarizations at the wavelength of (a) 800 nm, (b) 840 nm, (c) 920 nm, and (d) 980 nm.

The orientation angle accuracy $\Delta\psi$ and the ellipticity angle accuracy $\Delta\chi$ at each wavelength and the overall accuracy are written in Table 5.2. Orientation angles for the case of the RCP and LCP incidence are excluded because orientation angles of the given SOPs cannot be defined. Deviation angles of the both orientation and ellipticity are about 5 degrees.

Table 5.2 Measurement accuracies at each wavelength and the overall.

Wavelength (nm)	$\Delta\psi$ (°)	$\Delta\chi$ (°)
800	4.02	5.81
840	4.86	3.46
920	5.75	4.20
980	6.25	3.08
Total	**5.28**	**4.27**

5.4.3 Analysis on the accuracy: the parameters c and δ and size factor
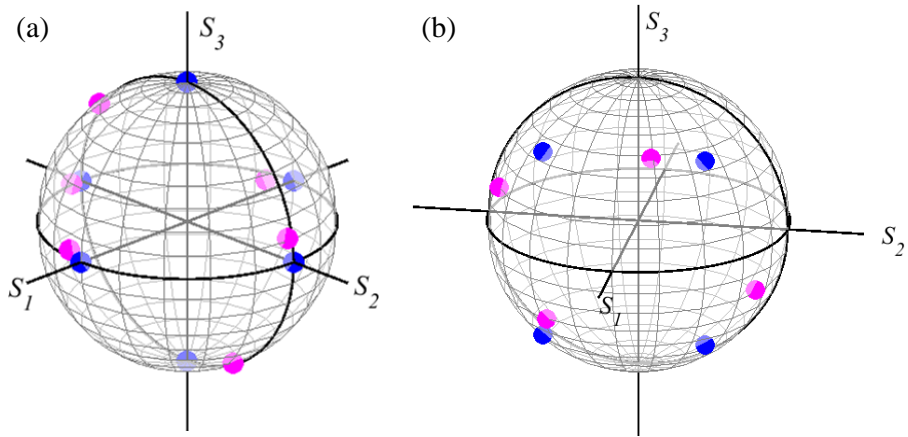
Figure 5.18 Poincaré sphere representation of the measured SOPs for (a) linear/circular polarizations and (b) elliptical polarizations at the wavelength of 760 nm.

Figure 5.18 shows the measured SOPs at the same set of given SOPs as in Figures 5.16 and 5.17 at the wavelength of 760 nm. It is seen that deviations

from the reference SOPs are larger than the case of the other wavelengths. The accuracies $\Delta\psi$ and $\Delta\chi$ are 7.92 ° and 11.28 °, which are 1.50 and 2.64 times larger than the overall accuracies of the polarimeter. This analysis implies that it is reasonable approach to design the X-shaped aperture array and the polarimeter according to the criteria proposed in Section 5.3.2. The accuracy of the polarimeter can be aggravated when c and δ get closer to the forbidden values.
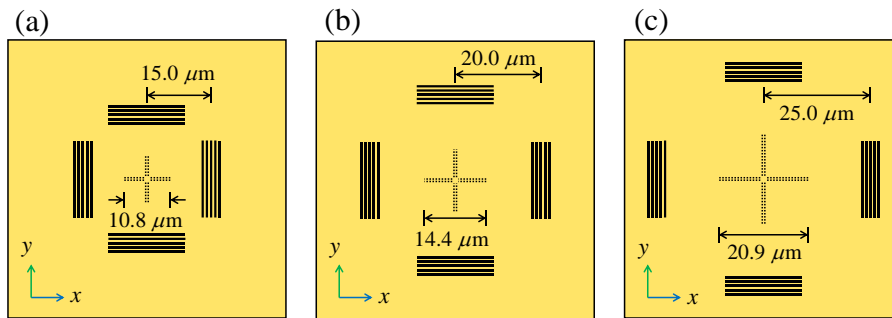
Figure 5.19 Top views of the polarimeter with different arm lengths that correspond to (a) 14, (b) 19, and (c) 28 periods.

The number of periods of the X-shaped aperture array, which composes each arm of the polarizer, can affect the accuracy. The accuracies are obtained from the measurement using 10 different SOPs, the same as done in the previous section. The period numbers of 14, 17, and 28 are tested, which correspond to arm lengths of 4.7 μm, 6.5 μm, and 9.7 μm. Figure 5.19 shows schematic illustrations of the polarimeters with different size factors. Note that the last case is the sample presented in the previous section.

(a) $n_y = 14, \chi = 45\,°$

$\lambda_0 = 800$ nm $\qquad$ $\lambda_0 = 840$ nm $\qquad$ $\lambda_0 = 920$ nm $\qquad$ $\lambda_0 = 980$ nm

(a) $n_y = 19, \chi = 45\,°$

$\lambda_0 = 800$ nm $\qquad$ $\lambda_0 = 840$ nm $\qquad$ $\lambda_0 = 920$ nm $\qquad$ $\lambda_0 = 980$ nm
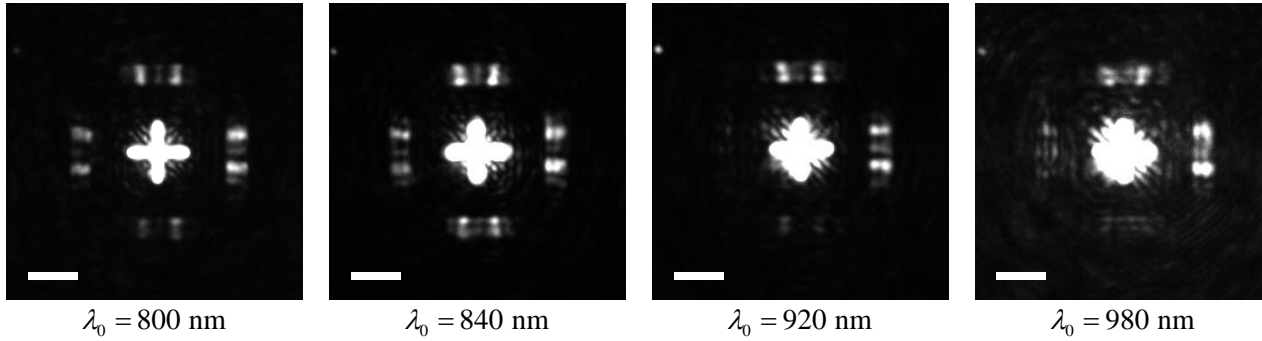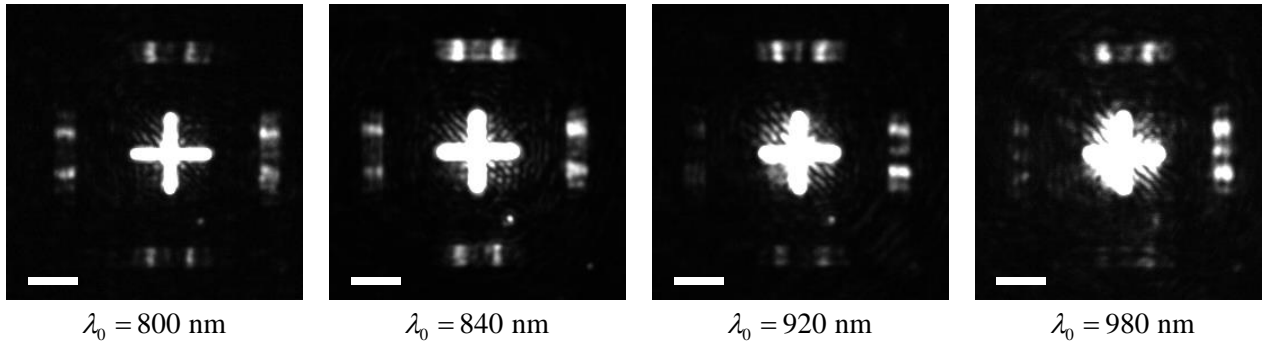
Figure 5.20 Captured images of the polarimeters with the period number (a) 14 and (b) 19 when illuminated by the RCP at each wavelength. Scale bars are 10 μm.

Table 5.3 Measurement accuracies at each wavelength and the overall wavelengths according to the arm length of the polarimeter.

Wavelength (nm)	$n_y = 14$		$n_y = 19$		$n_y = 28$	
	$\Delta\psi$ (°)	$\Delta\chi$ (°)	$\Delta\psi$ (°)	$\Delta\chi$ (°)	$\Delta\psi$ (°)	$\Delta\chi$ (°)
800	21.09	10.53	8.32	6.61	4.02	5.81
840	3.06	3.82	3.55	5.38	4.86	3.46
920	16.11	7.08	13.77	3.99	5.75	4.20
980	7.94	4.10	16.79	10.11	6.25	3.08
Total	**13.93**	**6.94**	**11.76**	**6.91**	**5.28**	**4.27**

Table 5.3 shows change of the accuracies according to the number of periods n_y. The deviations decreases as the period number increases. That is, the larger the footprint of the device is, the more precise the measurement. According to important factors of a certain application, the number of period can be adjusted.

5.5 Summary and discussions

In this chapter, a compact plasmonic polarimeter is proposed based on the X-shaped aperture array. Surface plasmon polaritons excited by the X-shaped aperture array are turned off at a given elliptical polarization state. In other words, the X-shaped aperture array can be modeled as an elliptical polarizer for SPPs. A polarimeter is composed of the X-shaped aperture array with vertical and horizontal arrangements, which are equivalent to superposition of four different elliptical polarizers. Polarization state of a normally incident light can be specified at a single detection of SPP intensities to each direction. Simulation results verify that an operation bandwidth of the polarimeter covers from 750 nm to 1050 nm. It is experimentally demonstrated that the proposed polarimeter can find out polarization angles with accuracy within 5 ° deviations. Design rules are proposed with regard to the accuracy of the polarimeter.

It is worthy of noting that the proposed polarimeter can easily be extended to other wavelengths by changing the geometry of the X-shaped aperture. Due to small footprint of the polarimeter, it can be applied to map spatial distribution of polarization states by scanning non-uniform optical beams, rather than averaging out the spatial distribution. Furthermore, the proposed polarimeter can be applied to more integrated detector, by replacing outcouplers to Schottky contacts [69]. The accuracy can be enhanced if measuring polarization states is located at the optima, which is represented by a regular tetrahedron inscribed in the Poincaré sphere [102]. In terms of the calibration factors used in this chapter, the regular tetrahedron

can be achieved when: $c = 1.932$, and $\delta = 45\ °$.

Chapter 6 Conclusion

In this dissertation, methods for polarization control of SPPs and their application to a compact polarimeter are discussed. Starting from interaction between polarized light and rectangular aperture array, a hybrid aperture pair array and an X-shaped aperture array are introduced that extends controllability using polarization states of incident light. Interferometry-controlled plasmonic resonator, directional launching and switching of SPPs using elliptically polarized light, and a compact polarimeter are proposed and demonstrated experimentally.

In Chapter 3, a plasmonic resonator is designed and demonstrated whose electromagnetic energy density can be controlled by the orientation angle of the incident electric field. Interferometric control of SPPs, which are excited by the nano-aperture pairs, makes the resonator tunable. After optimizing the resonator, the on/off ratio reaches 430. Based on the working principle of our work, interferometric control is possible without exquisite alignment of optical path length. That is, experimental setup of the interferometry can be significantly simplified. The proposed method can contribute to realizing all-optically controlled active plasmonic devices and coherent network elements.

In Chapter 4, directional launching and switching of SPPs using elliptically polarized light is investigated. A hybrid aperture pair array, which is composed of two sets of pair arrays with different size factor, is proposed. Polarization angles of both an orientation and an ellipticity angle are utilized

as a control variable, extending the controllability shown in the previous chapter. Experimental results show that directional launching can be achieved as predicted, as well as high extinction ratios. Here, a set of polarization states that can switch a direction of SPPs does not have to be orthogonal to each other. Hence, polarization control is possible with more diversity, other than binary operation.

In Chapter 5, a compact plasmonic polarimeter is proposed based on the X-shaped aperture array. A polarimeter is composed of the X-shaped aperture array with vertical and horizontal arrangements, which are equivalent to superposition of four different elliptical polarizers. Polarization state of a normally incident light can be specified at a single detection of SPP intensities to each direction. Simulation results verify that an operation bandwidth of the polarimeter covers from 750 nm to 1050 nm. It is experimentally demonstrated that the proposed polarimeter can find out polarization angles with accuracy within 5 ° deviations, wavelengths from 800 nm to 1000 nm. It is worthy of noting that the proposed polarimeter can easily be extended to other wavelengths by changing the geometry of the X-shaped aperture. Due to small footprint of the polarimeter, it can be applied to map spatial distribution of polarization states by scanning non-uniform optical beams, rather than averaging out the spatial distribution. Furthermore, the proposed polarimeter can be applied to more integrated detector. The accuracy can be enhanced if measuring polarization states is located at the optima, which is represented by a regular tetrahedron inscribed in the Poincaré sphere.

I expect that this dissertation can help to develop more compact optical

systems based on polarization-sensitive building blocks. Furthermore, I hope that this work inspires research on optical angular momentum interaction mediated by surface waves. More elaborate descriptions about spin-orbit interaction of light can be made if elliptically polarized light and intrinsic spin of surface waves are taken into account.

Bibliography

1. M. L. Brongersma and V. M. Shalaev. "The case for plasmonics," Science **328**(5977), 440–441 (2010).

2. K. F. MacDonald and N. I. Zheludev. "Active plasmonics: current status," Laser Photon. Rev. **4**(4), 562–567 (2010).

3. S. A. Maier and H. A. Atwater. "Plasmonics: Localization and guiding of electromagnetic energy in metal/dielectric structures," J. Appl. Phys. **98**(1), 011101 (2005).

4. Y. Fang and M. Sun. "Nanoplasmonic waveguides: towards applications in integrated nanophotonic circuits," Light Sci. Appl. **4**(6), e294 (2015).

5. S. A. Maier, G. K. Pieter, and H. A. Atwater. "Observation of coupled plasmon-polariton modes in Au nanoparticle chain waveguides of different lengths: Estimation of waveguide loss," Appl. Phys. Lett. **81**(9), 1714–1716 (2002).

6. S. I. Bozhevolnyi, V. S. Volkov, E. Devaux, J.-Y. Laluet, and T. W. Ebbesen, "Channel plasmon subwavelength waveguide components including interferometers and ring resonators," Nature **440**(7083), 508–511 (2006).

7. I.-M. Lee, J. Jung, J. Park, H. Kim, and B. Lee, "Dispersion characteristics of channel plasmon polariton waveguides with step-trench-type grooves," Opt. Express **15**(25), 16596-16603 (2007).

8. H. Ditlbacher, A. Hohenau, D. Wagner, U. Kreibig, M. Rogers, F. Hofer, F. Ausseneff, and J. R. Krenn, "Silver nanowires as surface plasmon resonators," Phys. Rev. Lett. **95**(25), 257403 (2005).

9. H. T. Miyazaki and K. Yoichi, "Squeezing visible light waves into a 3-nm-thick and 55-nm-long plasmon cavity," Phys. Rev. Lett. **96**(9), 097401 (2006).

10. J.-C. Weeber, A. Bouhelier, C. der Francs, L. Markey, and A. Dereux, "Submicrometer in-plane integrated surface plasmon cavities," Nano Lett. **7**(5), 1352–1359 (2007).

11. B. Min, E. Ostby, V. Sorger, E. Ulin-Avila, L. Yang, X. Zhang, and K. Vahala, "High-Q surface-plasmon-polariton whispering-gallery microcavity," Nature **457**(7228), 455–458 (2009).

12. D. Choi, I.-M. Lee, J. Jung, J. Park, J.-H. Han, and B. Lee, "Metallic-grating-based interconnector between surface plasmon polariton waveguides," J. Lightw. Technol. **27**(24), 5675–5680 (2009).

13. S.-Y. Lee, J. Park, M. Kang, and B. Lee, "Highly efficient plasmonic interconnector based on the asymmetric junction between metal-dielectric-metal and dielectric slab waveguides," Opt. Express **19**(10), 9562–9574 (2011).

14. S.-Y. Lee, J. Kim, I.-M. Lee, and B. Lee, "Efficient transition between photonic and plasmonic guided modes at abrupt junction of MIM plasmonic waveguide," Opt. Express **21**(18), 20762–20770 (2013).

15. R. J. Walters, R. V. A. V. Loon, I. Brunets, J. Schmitz, and A. Polman, "A silicon-based electrical source of surface plasmon polaritons," Nat. Mater **9**(1), 21–25 (2010).

16. R.-M. Ma, R. F. Oulton, V. J. Sorger, G. Bartal, and X. Zhang, "Room-temperature sub-diffraction-limited plasmon laser by total internal reflection," Nat. Mater. **10**(2), 110–113 (2011).

17. Y.-J. Lu, J. Kim, H. Y. Chen, C. Wu, N. Dabidian, C. E. Sanders, C.-Y. Wang, M.-Y. Lu, B.-H. Li, X. Qiu, W.-H. Chang, L.-J. Chen, G. Shvets, C.-K. Shih, and S. Gwo, "Plasmonic nanolaser using epitaxially grown silver film," Science **337**(6093), 450–453 (2012).

18. P. Fan, C. Colombo, K. C. Y. Huang, P. Krogstrup, J. Nygård, A. F. i Morral, and M. L. Brongersma, "An electrically-driven GaAs nanowire surface plasmon source," Nano Lett. **12**(9), 4943–4947 (2012).

19. D. Saxena, S. Mokkapati, P. Parkinson, N. Jiang, Q. Gao, H. H. Tan, and C. Jagadish, "Optically pumped room-temperature GaAs nanowire lasers," Nat. Photon. **7**(12), 963-968 (2013).

20. Q. Zhang, G. Li, X. Liu, F. Qian, Y. Li, T. C. Sum, C. M. Lieber, and Q. Xiong, "A room temperature low-threshold ultraviolet plasmonic nanolaser," Nat. Commun. **5**, 4953 (2014).

21. I. D. Leon and P. Berini. "Amplification of long-range surface plasmons by a dipolar gain medium," Nat. Photon. **4**(6), 382–387 (2010).

22. S. Kéna-Cohen, P. N. Stavrinou, D. D. Bradley, and S. A. Maier, "Confined surface plasmon-polariton amplifiers," Nano Lett. **13**(3), 1323–1329 (2013).

23. K. F. MacDonald, Z. L. Sámson, M. I. Stockman, and N. I. Zheludev, "Ultrafast active plasmonics," Nat. Photon. **3**(1), 55–58 (2009).

24. W. Cai, J. S. White, and M. L. Brongersma. "Compact, high-speed and power-efficient electrooptic plasmonic modulators," Nano Lett. **9**(12), 4403–4411 (2009).

25. A. V. Krasavin, T. P. Vo, W. Dickson, P. M. Bolger, and A. V. Zayats, "All-plasmonic modulation via stimulated emission of copropagating

surface plasmon polaritons on a substrate with gain," Nano Lett. **11**(6), 2231–2235 (2011).

26. A. Melikyan, L. Alloatti, A. Muslija, D. Hillerkuss, P. C. Schindler, J. Li, R. Palmer, D. Korn, S. Muehlbrandt, D. V. Thourhout, B. Chen, R. Dinu, M. Sommer, C. Koos, M. Kohl, W. Freude, and J. Leuthold, "High-speed plasmonic phase modulators," Nat. Photon. **8**(3), 229–233 (2014).

27. B. S. Dennis, M. I. Haftel, D. A. Czaplewski, D. Lopez, G. Blumberg, and V. A. Aksyuk, "Compact nanomechanical plasmonic phase modulators," Nat. Photon. **9**(4), 267–273 (2015).

28. D. E. Chang, A. S. Sørensen, E. A. Demler, and M. D. Lukin, "A single-photon transistor using nanoscale surface plasmons," Nat. Phys. **3**(11), 807–812 (2007).

29. R. A. Pala, K. T. Shimizu, N. A. Melosh, and M. L. Brongersma, "A nonvolatile plasmonic switch employing photochromic molecules," Nano Lett. **8**(5), 1506–1510 (2008).

30. J. A. Dionne, K. Diest, L. A. Sweatlock, and H. A. Atwater, "PlasMOStor: a metal− oxide− Si field effect plasmonic modulator," Nano Lett. **9**(2), 897–902 (2009).

31. H. P. Paudel, and M. N. Leuenberger, "Light-controlled plasmon switching using hybrid metal-semiconductor nanostructures," Nano Lett. **12**(6), 2690–2696 (2012).

32. H. Wei, Z. Wang, X. Tian, M. Käll, and H. Xu, "Cascaded logic gates in nanophotonic plasmon networks," Nat. Commun. **2**, 387 (2011).

33. Y. Fu, X. Hu, C. Lu, S. Yue, H. Yang, and Q. Gong, "All-optical logic gates based on nanoscale plasmonic slot waveguides," Nano Lett. **12**(11),

5784–5790 (2012).

34. L. Novotny and N. V. Hulst, "Antennas for light," Nat. Photon. **5**(2), 83–90 (2011).

35. Y. Liu, S. Palomba, Y. Park, T. Zentgraf, X. Yin, and X. Zhang, "Compact magnetic antennas for directional excitation of surface plasmons," Nano Lett. **12**(9), 4853–4858 (2012).

36. D. Vercruysse, Y. Sonnefraud, N. Verellen, F. B. Fuchs, G. Di Martino, L. Lagae, V. V. Moshchalkov, S. A. Maier, and P. V. Dorpe, "Unidirectional side scattering of light by a single-element nanoantenna," Nano Lett. **13**(8), 3843–3849 (2013).

37. X. Huang and M. L. Brongersma. "Compact aperiodic metallic groove arrays for unidirectional launching of surface plasmons," Nano Lett 13(11) 5420–5424 (2013).

38. J. Yang, X. Xiao, C. Hu, W. Zhang, S. Zhou, and J. Zhang, "Broadband surface plasmon polariton directional coupling via asymmetric optical slot nanoantenna pair," Nano Lett. **14**(2), 704–709 (2014).

39. J. Chen, C. Sun, H. Li, and Q. Gong, "Ultra-broadband unidirectional launching of surface plasmon polaritons by a double-slit structure beyond the diffraction limit," Nanoscale **6**(22), 13487–13493 (2014).

40. W. Yao, S. Liu, H. Liao, Z. Li, C. Sun, J. Chen, and Q. Gong, "Efficient directional excitation of surface plasmons by a single-element nanoantenna," Nano Lett, **15**(5), 3115–3121 (2015).

41. J. Chen, C. Sun, K. Rong, H. Li, and Q. Gong, "Polarization-free directional coupling of surface plasmon polaritons," Laser Photon. Rev. **9**(4), 419–426 (2015).

42. A. Pors, M. G. Nielsen, T. Bernardin, J.-C. Weeber, and S. I. Bozhevolnyi, "Efficient unidirectional polarization-controlled excitation of surface plasmon polaritons," Light Sci. Appl. **3**(8), e197 (2014).

43. Y. Shen, G. Fang, A. Cerjan, Z. Chi, S. Fan, and C. Jin, "Slanted gold mushroom array: a switchable bi/tridirectional surface plasmon polariton splitter," Nanoscale, **8**(34), 15505–15513 (2016).

44. S.-Y. Lee, I.-M. Lee, J. Park, S. Oh, W. Lee, K. Y. Kim, and B. Lee, "Role of magnetic induction currents in nanoslit excitation of surface plasmon polaritons," Phys. Rev. Lett. **108**(21), 213907 (2012).

45. G. M. Lerman and U. Levy. "Pin cushion plasmonic device for polarization beam splitting, focusing, and beam position estimation," Nano Lett. **13**(3), 1100–1105 (2013).

46. J. Lin, J. P. B. Mueller, Q. Wang, G. Yuan, N. Antoniou, X.-C. Yuan, and F. Capasso, "Polarization-controlled tunable directional coupling of surface plasmon polaritons," Science **340**(6130), 331-334 (2013).

47. L. Huang, X. Chen, B. Bai, Q. Tan, G. Jin, T. Zentgraf, and S. Zhang, "Helicity dependent directional surface plasmon polariton excitation using a metasurface with interfacial phase discontinuity," Light Sci. Appl. **2**(3), e70 (2013).

48. J. Yang, S. Zhou, C. Hu, W. Zhang, X. Xiao, and J. Zhang, "Broadband spin-controlled surface plasmon polariton launching and radiation via L-shaped optical slot nanoantennas," Laser Photon. Rev. **8**(4), 590–595 (2014).

49. Q. Jiang, A. Pham, M. Berthel, S. Huant, J. Bellessa, C. Genet, and A. Drezet, "Directional and singular surface plasmon generation in chiral

and achiral nanostructures demonstrated by Leakage Radiation Microscopy," ACS Photon. **3**(6), 1116–1124 (2016).

50. S.-Y. Lee, H. Yun, Y. Lee, and B. Lee, "Switchable surface plasmon dichroic splitter modulated by optical polarization," Laser Photon. Rev. **8**(5), 777–784 (2014).

51. K.Y. Bliokh, F. J. Rodríguez-Fortuño, F. Nori, and A. V. Zayats, "Spin-orbit interactions of light," Nat. Photon. **9**(12), 796–808 (2015).

52. H. Kim, J. Park, S.-W. Cho, S.-Y. Lee, M. Kang, and B. Lee, "Synthesis and dynamic switching of surface plasmon vortices with plasmonic vortex lens," Nano Lett. **10**(2), 529–536 (2010).

53. N. Shitrit, I. Bretner, Y. Gorodetski, V. Kleiner, and E. Hasman, "Optical spin Hall effects in plasmonic chains," Nano Lett. **11**(5), 2038–2042 (2011).

54. C.-F. Chen, C.-T. Ku, Y.-H. Tai, P.-K. Wei, H.-N. Lin, and C.-B. Huang, "Creating optical near-field orbital angular momentum in a gold metasurface," Nano Lett. **15**(4), 2746–2750 (2015).

55. S.-Y. Lee, K. Kim, S.-J. Kim, H. Park, K.-Y. Kim, and B. Lee, "Plasmonic meta-slit: shaping and controlling near-field focus," Optica 2(1), 6–13 (2015).

56. S.-Y. Lee, K. Kim, G.-Y. Lee, and B. Lee, "Polarization-multiplexed plasmonic phase generation with distributed nanoslits," Opt. Express 23(12), 15598–15607 (2015).

57. S.-Y. Lee, S.-J. Kim, H. Kwon, and B. Lee, "Spin-direction control of high-order plasmonic vortex with double-ring distributed nanoslits," IEEE Photon. Technol. Lett. 27(7), 705–708 (2015).

58. E.-Y. Song, S.-Y. Lee, J. Hong, K. Lee, Y. Lee, G.-Y. Lee, H. Kim, and B. Lee, "A double-lined metasurface for plasmonic complex-field generation," Laser Photon. Rev. 10(2), 299–306 (2016).

59. Y. D. Chong, L. Ge, H. Cao, and A. D. Stone, "Coherent perfect absorbers: time-reversed lasers," Phys. Rev. Lett. **105**(5), 053901 (2010).

60. W. Wan, Y. Chong, L. Ge, H. Noh, A. D. Stone, and H. Cao, "Time-reversed lasing and interferometric control of absorption," Science **331**(6019), 889–892 (2011).

61. J. Zhang, K. F. MacDonald, and N. I. Zheludev, "Controlling light-with-light without nonlinearity," Light Sci. Appl. **1**(7), e18 (2012).

62. R. Bruck and O. L. Muskens, "Plasmonic nanoantennas as integrated coherent perfect absorbers on SOI waveguides for modulators and all-optical switches," Opt. Express **21**(23), 27662–27671 (2013).

63. H. Park, S.-Y. Lee, J. Kim, B. Lee, and H. Kim, "Near-infrared coherent perfect absorption in plasmonic metal-insulator-metal waveguide," Opt. Express **23**(19), 24464–24474 (2015).

64. R. M. Azzam, I. M. Elminyawi, and A. N. El-Saba, "General analysis and optimization of the four-detector photopolarimeter," J. Opt. Soc. Am. A **5**(5), 681–689 (1988).

65. R. M. Matchko and G. R. Gerhart, "High-speed imaging chopper polarimetry," Opt. Eng. **47**(1), 016001 (2008).

66. W. Chen, D. C. Abeysinghe, R. L. Nelson, and Q. Zhan, "Experimental confirmation of miniature spiral plasmonic lens as a circular polarization analyzer," Nano Lett. **10**(6), 2075–2079 (2010).

67. K. A. Bachman, J. J. Peltzer, P. D. Flammer, T. E. Furtak, R. T. Collins,

and R. E. Hollingsworth, "Spiral plasmonic nanoantennas as circular polarization transmission filters," Opt. Express **20**(2), 1308–1319 (2012).

68. W. Li, Z. J. Coppens, L. V. Besteiro, W. Wang, A. O. Govorov, and J. Valentine, "Circularly polarized light detection with hot electrons in chiral plasmonic metamaterials," Nat. Commun. **6**, 8379 (2015).

69. F. Afshinmanesh, J. S. White, W. Cai, and M. L. Brongersma, "Measurement of the polarization state of light using an integrated plasmonic polarimeter," Nanophotonics **1**(2), 125–129 (2012).

70. Y.-B. Xie, Z.-Y. Liu, Q.-J. Wang, Y.-Y. Zhu, and X.-J. Zhang, "Miniature polarization analyzer based on surface plasmon polaritons," Appl. Phys. Lett. **105**(10), 101107 (2014).

71. A. Pors, M. G. Nielsen, and S. I. Bozhevolnyi, "Plasmonic metagratings for simultaneous determination of Stokes parameters," Optica **2**(8), 716–723 (2015).

72. J. P. B. Mueller, K. Leosson, and F. Capasso, "Ultracompact metasurface in-line polarimeter," Optica **3**(1), 42–47 (2016).

73. A. Espinosa-Soria, F. J. Rodriguez-Fortuno, A. Griol, and A. Martínez, "On-chip optimal Stokes nanopolarimetry based on spin-orbit interaction of light," Nano Lett. **17**(5) 3139–3144 (2017).

74. E. Maguid, I. Yulevich, D. Veksler, V. Kleiner, M. L. Brongersma, and E. Hasman, "Photonic spin-controlled multifunctional shared-aperture antenna array," Science **352**(6290), 1202–1206 (2016).

75. F. Ding, A. Pors, Y. Chen, V. A. Zenin, and S. I. Bozhevolnyi, "Beam-size-invariant spectropolarimeters using gap-plasmon metasurfaces," ACS Photon. **4**(4), 943–949 (2017).

76. P. J. Compaijen, V. A. Malyshev, and J. Knoester, "Elliptically polarized modes for the unidirectional excitation of surface plasmon polaritons," Opt. Express **24**(4), 3858–3872 (2016).

77. S. Maier, *Plasmonics: Fundamentals and Applications* (Springer, 2007).

78. T. W. Ebbesen, H. J. Lezec, H. F. Ghaemi, T. Thio, and P. A. Wolff, "Extraordinary optical transmission through sub-wavelength hole arrays," Nature **391**(6668), 667–669 (1998).

79. J. V. Coe, J. M. Heer, S. Teeters-Kennedy, H. Tian, and K. R. Rodriguez, "Extraordinary transmission of metal films with arrays of subwavelength holes," Annu. Rev. Phys. Chem. **59**, 179–202 (2008).

80. B. Lee, I.-M. Lee, S. Kim, D.-H. Oh, and L. Hesselink, "Review on subwavelength confinement of light with plasmonics," J. Mod. Opt. **57**(16), 1479–1497 (2010).

81. B. Luk'yanchuk, N. I. Zheludev, S. A. Maier, N. J. Halas, P. Nordlander, H. Giessen, and C. T. Chong, "The Fano resonance in plasmonic nanostructures and metamaterials," Nat. Mater. **9**(9), 707–715 (2010).

82. H. Liu and P. Lalanne, "Microscopic theory of the extraordinary optical transmission," Nature **452**(7188), 728–731 (2008).

83. N. Yu, P. Genevet, M. A. Kats, F. Aieta, J.-P. Tetienne, F. Capasso, and Z. Gaburro, "Light propagation with phase discontinuities: generalized laws of reflection and refraction," Science **334**(6054), 333–337 (2011).

84. Y. Zhao and A. Alù, "Tailoring the dispersion of plasmonic nanorods to realize broadband optical meta-waveplates," Nano Lett. **13**(3), 1086–1091 (2013).

85. S. Sun, K.-Y. Yang, C.-M. Wang, T.-K. Juan, W. T. Chen, C. Y. Liao, Q.

he, S. Xiao, W.-T. Kung, G.-Y. Guo, L. Zhou, and D. P. Tsai, "High-efficiency broadband anomalous reflection by gradient meta-surfaces," Nano Lett. **12**(12), 6223–6229 (2012).

86. N. Yu and F. Capasso, "Flat optics with designer metasurfaces," Nat. Mater. **13**(2), 139–150 (2014).

87. G. Zheng, H. Mühlenbernd, M. Kenney, G. Li, T. Zentgraf, and S. Zhang, "Metasurface holograms reaching 80 % efficiency," Nat. Nanotech. **10**(4), 308–312 (2015).

88. E.-Y. Song, G.-Y. Lee, H. Park, K. Lee, J. Kim, J. Hong, H. Kim, and B. Lee, "Compact Generation of Airy Beams with C-Aperture Metasurface," Adv. Opt. Mater. **5**(10), 1601028 (2017).

89. A. Archambault, T. V. Teperik, F. Marquier, and J. J. Greffet, "Surface plasmon Fourier optics," Phys. Rev. B **79**(19), 195414 (2009).

90. M. J. Weber, *Handbook of Optical Materials* (CRC, 2003).

91. M. T. Hill and M. C. Gather, "Advances in small lasers," Nat. Photon. **8**(12), 908–918 (2014).

92. V. J. Sorger, R. F. Oulton, J. Yao, G. Bartal, and X. Zhang, "Plasmonic Fabry-Pérot nanocavity," Nano Lett. **9**(10), 3489–3493 (2009).

93. K. J. Russell, T.-L. Liu, S. Cui, and E. L. Hu, "Large spontaneous emission enhancement in plasmonic nanocavities," Nat. Photon. **6**(7), 459–462 (2012).

94. C. Sauvan, J. P. Hugonin, I. S. Maksymov, and P. Lalanne, "Theory of the spontaneous optical emission of nanosize photonic and plasmon resonators," Phys. Rev. Lett. **110**(23), 237401 (2013).

95. R.-M. Ma, R. F. Oulton, Y. J. Sorger, and X. Zhang, "Plasmon lasers:

coherent light source at molecular scales," Laser Photon. Rev. **7**(1), 1–21. (2013).

96. K. Hassan, J.-C. Weeber, L. Markey, and A. Dereux, "Thermo-optical control of dielectric loaded plasmonic racetrack resonators," J. Appl. Phys. **110**(2), 023106 (2011).

97. V. W. Brar, M. S. Jang, M. Sherrott, J. J. Lopez, and H. A. Atwater, "Highly confined tunable mid-infrared plasmonics in graphene nanoresonators," Nano Lett. **13**(6), 2541–2547 (2013).

98. L. Novotny and B. Hecht, *Principles of Nano-Optics* (Cambridge University, 2012).

99. T. Zentgraf, Y. Liu, M. H. Mikkelsen, J. Valentine, and X. Zhang, "Plasmonic Luneburg and Eaton lenses," Nat. Nanotech. **6**(3), 151–155 (2011).

100. H. Wei, Z. Li, X. Tian, Z. Wang, F. Cong, N. Liu, S. Zhang, P. Nordlander, N. J. Halas, and H. Xu, "Quantum dot-based local field imaging reveals plasmon-based interferometric logic in silver nanowire networks," Nano Lett. **11**(2), 471–475 (2010).

101. H, Wei, Z. Wang, X. Tian, M. Käll, and H. Xu, "Cascaded logic gates in nanophotonic plasmon networks," Nat. Commun. **2**, 387 (2011).

102. R. M. A. Azzam, "Stokes-vector and Mueller-matrix polarimetry", J. Opt. Soc. Am. A **33**(7), 1396–1408 (2016).

Appendix

Portions of the work discussed in this dissertation are also presented in the following publications:

[Chapter 2] K. Lee, J. Kim, H. Yun, G.-Y. Lee, and B. Lee, "Interferometric control of plasmonic resonator based on polarization-sensitive excitation of surface plasmon polaritons," Opt. Express **24**(19), 21861–21868 (2016).

초   록

표면 플라즈몬 폴라리톤은 금속-유전체 경계면을 따라 진행하는 전자기파를 말한다. 표면 플라즈몬 폴라리톤은 파장 한계 이하의 구조에서도 집속되거나 도파하는 것이 가능하다. 이러한 특징은 광집적회로에 적용되기에 적합하여 지난 약 20년간 다양한 형태의 능동형, 수동형 표면 플라즈몬 폴라리톤 변조 소자가 연구되었다.

높은 결합 효율로 표면 플라즈몬 폴라리톤을 여기시키는 것은 여전히 주요한 이슈 중 하나로, 비대칭 구조물 및 비등방 산란을 이용한 표면 플라즈몬 폴라리톤의 방향 여기가 최근 주목을 받고 있다. 이와 더불어 방향 제어에 대한 연구 또한 적극적으로 제안되고 있다. 다양한 방향 제어 방법 중 입사광의 편광을 이용하는 방법이 있다. 편광을 이용한 표면 플라즈몬의 방향성 여기 및 그 제어 방법은 비등방 산란을 이용한 구조물에서 그 제어가 용이하다는 장점이 있다. 하지만 선편광 혹은 원편광 등 제한적인 편광 상태만을 사용함으로써 제어의 자유도가 크게 제약받고 있다.

본 박사학위 논문에서는 주기적으로 배열된 나노 개구 쌍을 이용하여 표면 플라즈몬의 방향 제어에 사용되는 편광 상태의 범위를 확장하고, 이를 응용한다.

첫번째 응용으로는 편광 회전각으로 제어 가능한 플라즈몬 공진기를 제안한다. 제안한 소자에서는 두 개의 마주보는 형태의 개구 쌍 배열을 이용, 서로 반대방향으로 발진하는 표면 플라즈몬 폴라리톤을 발생시킨다. 이때 표면 플라즈몬 폴라리톤 간 위상차가 입사광의 편광 회전각으로 조절되어 표면 플라즈몬 폴라리톤의 간

섭이 조절된다. 간섭 무늬와 공진기 간 상대적 위치에 따라 공진기 내 저장되는 전자기에너지가 제어된다. 이는 간섭을 통한 매질의 광특성 변조를 복잡한 광경로 조절 없이 편광 조절으로만 가능케 했다는 의의가 있다.

다음으로는 표면 플라즈몬 폴라리톤의 편광 의존적 여기 현상을 이용한 초소형 편광측정기를 제안한다. 편광측정기 구성에 앞서 타원 편광에서 표면 플라즈몬 폴라리톤의 방향 여기가 가능한 혼성 개구 쌍 배열과 십자형 개구 배열 구조를 제안한다. 제안된 혼성 개구 쌍 배열은 임의의 타원 편광에서 표면 플라즈몬 폴라리톤을 방향성을 갖게 여기 시킬 수 있다. 표면 플라즈몬 폴라리톤을 투과 광으로 보았을 때, 이는 제안한 소자가 타원 편광판의 기능을 수행함을 의미한다. 서로 다른 네 개의 타원 편광판에 해당하는 십자형 개구 배열을 배치함으로써 편광측정기를 구현할 수 있다. 제안된 편광측정기는 작은 소자에서 원샷 측정이 가능하다는 장점이 있다. 또한 약 200 nm 정도의 동작 대역폭을 실험적으로 확인하였다.

본 박사학위 논문의 결과는 편광 의존적 동작이 요구되는 각종 광 시스템의 개선과 소형화에 기여할 수 있을 것으로 기대된다. 또한 나노 구조물과 표면파로 촉발된 빛의 각운동량 상호작용에 대한 연구에도 활용될 수 있을 것으로 기대된다.

주요어: 표면 플라즈몬 폴라리톤, 편광 상태, 편광 변조 광소자, 파장한계 이하 구조, 비등방성 산란, 간섭 제어
학 번: 2012-20824